Image Analysis Using a Dual-Tree M-Band Wavelet Transform

Caroline Chaux, *Student Member*, Laurent Duval, *Member* and
Jean-Christophe Pesquet, *Senior Member, IEEE*

***Abstract*— We propose a 2D generalization to the M-band case of the dual-tree decomposition structure (initially proposed by N. Kingsbury and further investigated by I. Selesnick) based on a Hilbert pair of wavelets. We particularly address (*i*) the construction of the dual basis and (*ii*) the resulting directional analysis. We also revisit the necessary pre-processing stage in the M-band case. While several reconstructions are possible because of the redundancy of the representation, we propose a new optimal signal reconstruction technique, which minimizes potential estimation errors. The effectiveness of the proposed M-band decomposition is demonstrated via denoising comparisons on several image types (natural, texture, seismics), with various M-band wavelets and thresholding strategies. Significant improvements in terms of both overall noise reduction and direction preservation are observed.**

***Index Terms*— Wavelets, M-band filter banks, Hilbert transform, Dual-tree, Image denoising, Direction selection.**

I. Introduction

The classical discrete wavelet transform (DWT) provides a means of implementing a multiscale analysis, based on a critically sampled filter bank with perfect reconstruction. It has been shown to be very effective both theoretically and practically [3] in the processing of certain classes of signals, for instance piecewise smooth signals, having a finite number of discontinuities. But, while decimated transforms yield good compression performance, other data processing applications (analysis, denoising, detection) often require more sophisticated schemes than DWT.

One first drawback usually limiting the practical performance of DWT algorithms is their shift-variance with respect to the value of the transformed coefficients at a given scale. It often results in shift-variant edge artifacts at the vicinity of jumps, which are not desirable in real-world applications, signal delays being rarely known.

A second drawback arises in dimensions greater than one: tensor products of standard wavelets usually possess poor directional properties. The later problem is sensitive in feature detection or denoising applications. A vast majority of the proposed solutions relies on adding some redundancy to the transform. Redundancy based on shift-invariant wavelet transforms (see [4], [5] and references therein) suppresses shift dependencies, at the expense of an increased computational cost, which often becomes intractable in higher dimensions. Less computationally-expensive approaches have been developed on complex filters for real signals (we refer to [6] for an overview and design examples), or by employing other wavelet frames [7]. For instance, it is possible to resort to the concatenation of several wavelet bases. One of the most promising decomposition is the *dual-tree* discrete wavelet transform, proposed by N. Kingsbury [8]: two classical wavelet trees are developed in parallel, with filters forming (approximate) Hilbert pairs. Advantages of Hilbert pairs had been earlier recognized by other authors [9]. In the complex case, the resulting analysis yields a redundancy of only 2^d for d-dimensional signals, with a much lower shift sensitivity and better directionality in 2D than the DWT. The design of dual-tree filters is addressed in [10] through an approximate Hilbert pair formulation for the "dual" wavelets. I. Selesnick also proposed the double-density DWT and combined both frame approaches [11]. The *phaselet* extension of the dual-tree DWT has been recently introduced by R. Gopinath in [12]. More recently, several authors have also proposed a projection scheme with an explicit control of the redundancy or with specific filter bank structures [13], [14]. Finally, other works on the blending of analytic signals and wavelets must be mentioned [15], [16], in the context of denoising or higher dimension signal processing. Recent developments based on "geometrical" wavelets are not mentioned here, in spite of their relevance.

A third drawback concerns design limitations in two-band decompositions: orthogonality, realness, symmetry, compactness of the support and other properties (regularity, vanishing moments) compete. The relative sparsity of good filter banks amongst all possible solutions is also well-known. In order to improve both design freedom and filter behavior, M-band filter banks and wavelets have been proposed [17]–[19].

Improving on our previous work [1], we propose the construction of a 2D dual-tree M-band wavelet decomposition. The organization of the paper is as follow: in Section II, we investigate the theoretical conditions for the construction of M-band Hilbert pairs. In Section III, we extend previous results on the pre-processing stage to the M-band context and illustrate the direction extraction with the constructed wavelets. Since several reconstructions are possible, due to the decomposition redundancy, we then propose an optimal pseudo-inverse based frame reconstruction, which allows to reduce the effects of coefficient estimation errors. Implementation issues are discussed in Section IV. In Section V, we consider

Part of this work was presented at the 2004 EUSIPCO conference [1] and at the 2005 ICASSP conference [2].

C. Chaux and J.-C. Pesquet are with the Institut Gaspard Monge and CNRS-UMR 8049, Université de Marne-la-Vallée, 77454 Marne-la-Vallée Cedex 2, France. E-mail: {chaux,pesquet}@univ-mlv.fr.

L. Duval is with the Institut Français du Pétrole, Technology, Computer Science and Applied Mathematics Division, 92500 Rueil Malmaison, France. E-mail: laurent.duval@ifp.fr.

image denoising applications and provide experimental results showing significant improvements in terms of both noise reduction and direction preservation. Conclusions are drawn in Section VI.

II. Construction of M-band Hilbert pairs

A. Problem statement

In this section, we will focus on 1D signals belonging to the space $\mathrm{L}^2(\mathbb{R})$ of square integrable functions. Let M be an integer greater than or equal to 2. Recall that an M-band multiresolution analysis of $\mathrm{L}^2(\mathbb{R})$ is defined by one scaling function (or father wavelet) $\psi_0 \in \mathrm{L}^2(\mathbb{R})$ and $(M-1)$ mother wavelets $\psi_m \in \mathrm{L}^2(\mathbb{R})$, $m \in \{1,\ldots,M-1\}$ [18]. These functions are solutions of the following scaling equations:

$$\forall m \in \{0,\ldots,M-1\}, \quad \frac{1}{\sqrt{M}}\psi_m(\frac{t}{M}) = \sum_{k=-\infty}^{\infty} h_m[k]\psi_0(t-k), \quad (1)$$

where the sequences $(h_m[k])_{k\in\mathbb{Z}}$ are square integrable. In the following, we will assume that these functions (and thus the associated sequences $(h_m[k])_{k\in\mathbb{Z}}$) are real-valued. The Fourier transform of $(h_m[k])_{k\in\mathbb{Z}}$ is a 2π-periodic function, denoted by H_m. Thus, in the frequency domain, Eq. (1) can be re-expressed as:

$$\forall m \in \{0,\ldots,M-1\}, \ \sqrt{M}\widehat{\psi}_m(M\omega) = H_m(\omega)\widehat{\psi}_0(\omega), \quad (2)$$

where $\widehat{a}$ denotes the Fourier transform of a function a. For the set of functions $\cup_{m=1}^{M-1}\{M^{-j/2}\psi_m(M^{-j}t-k),(j,k)\in\mathbb{Z}^2\}$ to correspond to an orthonormal basis of $\mathrm{L}^2(\mathbb{R})$, the following para-unitarity conditions must hold:

$$\forall (m,m') \in \{0,\ldots,M-1\}^2, \quad \sum_{p=0}^{M-1} H_m(\omega+p\frac{2\pi}{M})H^*_{m'}(\omega+p\frac{2\pi}{M}) = M\delta_{m-m'}, \quad (3)$$

where $\delta_m = 1$ if $m=0$ and 0 otherwise. The filter with frequency response H_0 is low-pass whereas usually the filter with frequency response H_m, $m \in \{1,\ldots,M-2\}$ (resp. $m = M-1$) is band-pass (resp. high-pass). In this case, cascading the M-band para-unitary analysis and synthesis filter banks, depicted in the upper branch in Fig. 1, allows us to decompose and to reconstruct perfectly a given signal.

Our objective is to construct a "dual" M-band multiresolution analysis defined by a scaling function ψ_0^{H} and mother wavelets ψ_m^{H}, $m \in \{1,\ldots,M-1\}$. More precisely, the mother wavelets will be obtained by a Hilbert transform from the "original" wavelets ψ_m, $m \in \{1,\ldots,M-1\}$. In the Fourier domain, the desired property reads:

$$\forall m \in \{1,\ldots,M-1\}, \qquad \widehat{\psi}_m^{\mathrm{H}}(\omega) = -\imath\,\mathrm{sign}(\omega)\widehat{\psi}_m(\omega), \quad (4)$$

where sign is the signum function defined as:

$$\mathrm{sign}(\omega) = \begin{cases} 1 & \text{if } \omega > 0 \\ 0 & \text{if } \omega = 0 \\ -1 & \text{if } \omega < 0. \end{cases} \quad (5)$$

As it is common in wavelet theory, Eq. (4), as well as all equalities in the paper involving square integrable functions, holds almost everywhere (that is, for all $\omega \notin \Omega$ where Ω is a real set of zero measure).

Furthermore, the functions ψ_m^{H} are defined by scaling equations similar to (1) involving real-valued sequences $(g_m[k])_{k\in\mathbb{Z}}$:

$$\forall m \in \{0,\ldots,M-1\}, \quad \frac{1}{\sqrt{M}}\psi_m^{\mathrm{H}}(\frac{t}{M}) = \sum_{k=-\infty}^{\infty} g_m[k]\psi_0^{\mathrm{H}}(t-k) \quad (6)$$

$$\iff \sqrt{M}\widehat{\psi}_m^{\mathrm{H}}(M\omega) = G_m(\omega)\widehat{\psi}_0^{\mathrm{H}}(\omega). \quad (7)$$

In order to generate a dual M-band orthonormal wavelet basis of $\mathrm{L}^2(\mathbb{R})$, the Fourier transforms G_m of the sequences $(g_m[k])_{k\in\mathbb{Z}}$ must also satisfy the para-unitarity conditions:

$$\forall (m,m') \in \{0,\ldots,M-1\}^2, \quad \sum_{p=0}^{M-1} G_m(\omega+p\frac{2\pi}{M})G^*_{m'}(\omega+p\frac{2\pi}{M}) = M\delta_{m-m'}. \quad (8)$$

The corresponding para-unitary Hilbert filter banks are illustrated by the lower branch in Fig. 1.

B. Sufficient conditions for obtaining dual decompositions

The Hilbert condition (4) yields

$$\forall m \in \{1,\ldots,M-1\}, \qquad |\widehat{\psi}_m^{\mathrm{H}}(\omega)| = |\widehat{\psi}_m(\omega)|. \quad (9)$$

If we further impose that $|\widehat{\psi}_0^{\mathrm{H}}(\omega)| = |\widehat{\psi}_0(\omega)|$, the scaling equations (2) and (7) lead to

$$\forall m \in \{0,\ldots,M-1\}, \qquad G_m(\omega) = e^{-\imath\theta_m(\omega)}H_m(\omega), \quad (10)$$

where θ_m is 2π-periodic. The phase functions θ_m should also be odd (for real filters) and thus only need to be determined over $[0,\pi]$.

For any $(m,m') \in \{0,\ldots,M-1\}^2$ with $m < m'$, let $(\mathsf{P}_{m,m'})$ denote the following assumption: The function $\alpha_{m,m'} = \theta_{m'} - \theta_m$ is such that, for (almost) all $\omega \in [0,2\pi[$,

$$\alpha_{m,m'}(\omega+\frac{2\pi}{M}) = \alpha_{m,m'}(\omega) \pmod{2\pi}. \quad (11)$$

Assuming that Eq. (3) is satisfied, it is then straightforward to verify that the para-unitarity conditions (8) for the dual filter bank hold if $(\mathsf{P}_{m,m'})$ holds. We are then able to state the following result:

Proposition 1: Assume that Conditions (10) hold. A necessary and sufficient condition for Eq. (4) to be satisfied is that there exists $\tilde{\theta}_0 = \theta_0 \pmod{2\pi}$ such that

$$\beta(\omega) = \sum_{i=1}^{\infty} \tilde{\theta}_0\left(\frac{\omega}{M^i}\right) \quad (12)$$

is a convergent series and, $\forall m \in \{1,\ldots,M-1\}$,

$$\tilde{\alpha}_{0,m}\left(\frac{\omega}{M}\right) + \beta(\omega) = \frac{\pi}{2}\mathrm{sign}(\omega) \pmod{2\pi} \quad (13)$$

where $\tilde{\alpha}_{0,m} = \theta_m - \tilde{\theta}_0$.

Proof: Given that $\widehat{\psi}_0(0) = 1$, for $m = 0$ Eq. (2) is equivalent to

$$\widehat{\psi}_0(\omega) = \prod_{i=1}^{\infty}[\frac{1}{\sqrt{M}} H_0(\frac{\omega}{M^i})]. \quad (14)$$

Similarly, we have for the "dual" scaling function:

$$\widehat{\psi}_0^{\mathrm{H}}(\omega) = \prod_{i=1}^{\infty}[\frac{1}{\sqrt{M}} G_0(\frac{\omega}{M^i})]. \quad (15)$$

Furthermore, the expressions of the Fourier transforms of the mother wavelets and "dual" mother wavelets can be deduced from Eqs. (2) and (7). Consequently, Condition (4) may be rewritten as $\forall m \in \{1, \ldots, M-1\}$,

$$G_m(\frac{\omega}{M}) \prod_{i=2}^{\infty}[\frac{1}{\sqrt{M}} G_0(\frac{\omega}{M^i})] = - \imath \, \mathrm{sign}(\omega) H_m(\frac{\omega}{M}) \prod_{i=2}^{\infty}[\frac{1}{\sqrt{M}} H_0(\frac{\omega}{M^i})]. \quad (16)$$

Using Eq. (10), we see that the above relation is verified if and only if there exists $\tilde{\theta}_0 = \theta_0 \pmod{2\pi}$ such that

$$\forall m \in \{1, \ldots, M-1\}, \quad \theta_m(\frac{\omega}{M}) + \sum_{i=2}^{\infty} \tilde{\theta}_0(\frac{\omega}{M^i}) = \frac{\pi}{2}\mathrm{sign}(\omega) \pmod{2\pi}$$

where the involved series is convergent. The above equation is obviously equivalent to Eq. (13). ∎

Eqs. (13) and (12) constitute a generalization to the M-band case of a famous result by Selesnick [10] restricted to dyadic wavelets. One can remark that the convergence properties of the series $\beta(\omega)$ are only related to the behaviour of $\tilde{\theta}_0$ around the origin since $\omega/M^i \to 0$ as $i \to \infty$. It is also worth noting that the function β is given by the following "additive" scaling equation:

$$\beta(\omega) = \beta\left(\frac{\omega}{M}\right) + \tilde{\theta}_0\left(\frac{\omega}{M}\right). \quad (17)$$

C. Linear phase solution

In the 2-band case (under weak assumptions), $\tilde{\theta}_0$ verifying Eqs. (13) and (12) is a linear function on $[-\pi, \pi[$ [10]. In the M-band case, we will slightly restrict this constraint on a smaller interval by imposing:

$$\forall \omega \in [0, 2\pi/M[, \qquad \tilde{\theta}_0(\omega) = \gamma\omega, \quad (18)$$

where $\gamma \in \mathbb{R}$. This choice clearly guarantees that the series $\beta(\omega)$ is convergent. Using Eq. (17), after some calculations which are provided in Appendix I, the following result can be proved:

Proposition 2: Under the three conditions (10), $(\mathsf{P}_{0,m})_{m\geq 1}$ and (18), the solutions (modulo 2π) to Eq. (13) are given by

$$\forall m \in \{1, \ldots, M-1\}, \quad \tilde{\alpha}_{0,m}(\omega) = \begin{cases} \frac{\pi}{2} - (d + \frac{1}{2})M\omega & \text{if } \omega \in]0, \frac{2\pi}{M}[, \\ 0 & \text{if } \omega = 0. \end{cases} \quad (19)$$

and $\forall p \in \left\{0, \ldots, \left\lceil \frac{M}{2} \right\rceil - 1\right\}, \forall \omega \in \left[p\frac{2\pi}{M}, (p+1)\frac{2\pi}{M}\right[$,

$$\tilde{\theta}_0(\omega) = (d + \frac{1}{2})(M-1)\,\omega - p\pi, \quad (20)$$

where $d \in \mathbb{Z}$ and $\lceil u \rceil$ denotes the upper integer part of a real u.

The integer d defines a possible arbitrary delay between the filters of the original and dual decompositions. Up to this delay, Proposition 2 states that, subject to (10), $(\mathsf{P}_{0,m})_{m\geq 1}$ and (18), there exists a unique solution to Eq. (13). It should also be noted that except for the 2-band case, $\tilde{\theta}_0$ exhibits discontinuities on $]0, \pi[$ due to the $p\pi$ term (see Fig. 2). These discontinuities however occur at zeros of the frequency response of the lowpass filter since we have $H_0(2p\pi/M) = 0$, for all $p \in \{1, \ldots, M-1\}$ [18].

We subsequently deduce the following corollary of the above proposition:

Proposition 3: Para-unitary M-band Hilbert filter banks are obtained by choosing the phase functions defined by Eq. (20) and

$$\forall m \in \{1, \ldots, M-1\}, \quad \theta_m(\omega) = \begin{cases} \frac{\pi}{2} - \left(d + \frac{1}{2}\right)\omega & \text{if } \omega \in]0, 2\pi[, \\ 0 & \text{if } \omega = 0, \end{cases} \quad (21)$$

where $d \in \mathbb{Z}$. Then, the scaling function associated to the dual wavelet decomposition is such that

$$\forall k \in \mathbb{N}, \ \forall \omega \in [2k\pi, 2(k+1)\pi[, \quad \widehat{\psi}_0^{\mathrm{H}}(\omega) = (-1)^k e^{-\imath(d+\frac{1}{2})\omega} \, \widehat{\psi}_0(\omega). \quad (22)$$

Proof: It is readily shown that, if $\tilde{\theta}_0$ is given by Eq. (20), $\tilde{\alpha}_{0,m}$ is a $2\pi/M$-periodic function satisfying (almost everywhere) Eq. (19) if and only if the functions θ_m, $m \in \{1, \ldots, M-1\}$, are expressed by Eq. (21) (modulo 2π). Then, we conclude from Proposition 2 that the phases given by Eqs. (20)-(21) allow us to satisfy the Hilbert condition (13). Furthermore, the functions θ_m, $m \in \{1, \ldots, M-1\}$, being all equal, the paraunitary conditions $(\mathsf{P}_{m,m'})_{m'>m\geq 0}$ are obviously fulfilled. According to Eqs. (12), (14) and (15), $\widehat{\psi}_0^{\mathrm{H}}(\omega) = e^{-\imath\beta(\omega)} \, \widehat{\psi}_0(\omega)$. When $\tilde{\theta}_0$ takes the form (20), the expression of β is given by Eq. (65) in Appendix I, thus yielding Eq. (22). ∎

Note that in the dyadic case, necessary and sufficient conditions have been found for the linear phase property [20].

D. Compact support

Compactly supported wavelets are obtained with FIR (Finite Impulse Response) filters. However, if the filters with frequency responses $H_m(\omega)$ with $m \in \{1, \ldots, M-1\}$ are FIR (i.e. $H_m(\omega)$ is a Laurent polynomial in $e^{\imath\omega}$), the dual filters with frequency responses $G_m(\omega)$ cannot be FIR. Indeed, the $\omega/2$ term in Eq. (21) prevents $G_m(\omega)$ from being a polynomial or even a rational function in $e^{\imath\omega}$. When M is even, a similar argument holds showing that the low-pass filter $G_0(\omega)$ cannot be FIR if the primal one is FIR and Eq. (20) is satisfied. When M is odd, the jumps of π arising for $\tilde{\theta}_0$ at frequencies $2p\pi/M$ with $p \in \{1, \ldots, M-1\}$ allow us to draw the same conclusion.

In other words, starting from orthonormal compactly supported scaling functions/wavelets, it is not possible to generate dual basis functions having a compact support. However, the study of approximate FIR Hilbert pairs satisfying perfect reconstruction has been addressed by several authors in the dyadic case [21], [8].

E. Symmetry properties

As already pointed out, one of the main advantage of the M-band case with $M > 2$ is to allow the construction of non-trivial real orthonormal bases with compact support *and* symmetric (or antisymmetric) wavelets. Assume that symmetry properties are fulfilled for the primal filter bank. We now show that the dual filters and wavelets inherit these properties. Indeed, it can be proved (see Appendix II) that:

Proposition 4: Let phase conditions (20), (21) be satisfied. If the low-pass impulse response $(h_0[k])_{k\in\mathbb{Z}}$ is symmetric w.r.t. $k_0 \in \frac{1}{2}\mathbb{Z}$, and, for $m \in \{1,\dots,M-1\}$, $(h_m[k])_{k\in\mathbb{Z}}$ is symmetric (resp. antisymmetric) w.r.t. $k_m \in \frac{1}{2}\mathbb{Z}$, then $(g_0[k])_{k\in\mathbb{Z}}$ is symmetric w.r.t. $k_0 + (d+\frac{1}{2})(M-1)$ and $(g_m[k])_{k\in\mathbb{Z}}$ is antisymmetric (resp. symmetric) w.r.t. $k_m - d - \frac{1}{2}$.
Under the assumptions of the above proposition, Eqs. (14) and (2) allow us to claim that ψ_0 is symmetric w.r.t.

$$\tau = \frac{k_0}{M-1} \tag{23}$$

and, for $m \in \{1,\dots,M-1\}$, ψ_m is symmetric (resp. antisymmetric) w.r.t. $(\tau + k_m)/M$. Then, it is easily deduced from Eqs. (22) and (4) that ψ_0^{H} is symmetric w.r.t. $\tau + d + 1/2$ and, for $m \in \{1,\dots,M-1\}$, ψ_m^{H} is antisymmetric (resp. symmetric) w.r.t. $(\tau + k_m)/M$.

III. Extension to 2D dual-tree M-band wavelet analysis

A. 2D Decomposition

Two-dimensional separable M-band wavelet bases can be deduced from the 1D dual-tree decomposition derived in Section II. The so-obtained bases of $\mathrm{L}^2(\mathbb{R}^2)$ (the space of square integrable functions defined on $\mathbb{R}^2$) are

$$\bigcup_{j=-\infty}^{J} \bigcup_{\substack{(m,m')\\ \neq(0,0)}} \{M^{-j}\psi_m(\frac{x}{M^j}-k)\psi_{m'}(\frac{y}{M^j}-l),(k,l)\in\mathbb{Z}^2\}$$
$$\bigcup \{M^{-J}\psi_0(\frac{x}{M^J}-k)\psi_0(\frac{y}{M^J}-l),(k,l)\in\mathbb{Z}^2\} \tag{24}$$
$$\bigcup_{j=-\infty}^{J} \bigcup_{\substack{(m,m')\\ \neq(0,0)}} \{M^{-j}\psi_m^{\mathrm{H}}(\frac{x}{M^j}-k)\psi_{m'}^{\mathrm{H}}(\frac{y}{M^j}-l),(k,l)\in\mathbb{Z}^2\}$$
$$\bigcup \{M^{-J}\psi_0^{\mathrm{H}}(\frac{x}{M^J}-k)\psi_0^{\mathrm{H}}(\frac{y}{M^J}-l),(k,l)\in\mathbb{Z}^2\} \tag{25}$$

where $J \in \mathbb{Z}$ is the considered coarsest decomposition level. A discrete implementation of these wavelet decompositions starts from level $j = 1$ to $J \in \mathbb{N}^*$. As pointed out in the seminal works of Kingsbury and Selesnick, it is however advantageous to add some pre- and post-processing to this decomposition. The pre-processing aims at establishing the connection between the analog theoretical framework and its discrete-time implementation whereas the post-processing is used to provide directional analysis features to the decomposition. We will now revisit these problems in the context of M-band decompositions.

The proposed $2D$ M-band dual-tree decomposition is illustrated in Fig. 3. For the sake of simplicity, only two levels of decomposition ($J = 2$) are represented but this transform can be implemented over further levels, the approximation coefficients being re-decomposed iteratively. For each of the two M-band decompositions, we get $J\times M^2 - J + 1$ subbands. We observe that the $2D$ dual-tree decomposition can be divided into three steps which are detailed hereafter.

1) Prefiltering: The wavelet transform is a continuous-space formalism that we want to apply to a "discrete" image. We consider that the analog scene corresponds to the 2D field:

$$f(x,y) = \sum_{k,l} f[k,l]\; s(x-k,y-l) \tag{26}$$

where s is some interpolation function and $(f[k,l])_{(k,l)\in\mathbb{Z}^2}$ is the image sample sequence. Let us project the image onto the approximation space

$$V_0 = \overline{\mathrm{Span}}\{\psi_0(x-k)\psi_0(y-l),(k,l)\in\mathbb{Z}^2\}. \tag{27}$$

The projection of f reads

$$P_{V_0}(f(x,y)) = \sum_{k,l} c_{0,0,0}[k,l]\;\psi_0(x-k)\;\psi_0(y-l) \tag{28}$$

where the approximation coefficients are

$$c_{0,0,0}[k,l] = \langle f(x,y), \psi_0(x-k)\;\psi_0(y-l)\rangle \tag{29}$$

and $\langle\,,\,\rangle$ denotes the inner product of $\mathrm{L}^2(\mathbb{R}^2)$. Using Eq. (26) we obtain:

$$c_{0,0,0}[k,l] = \sum_{p,q} f[p,q]\;\gamma_{s,\Psi_{0,0}}(k-p,l-q) \tag{30}$$

where $\Psi_{0,0}(x,y) = \psi_0(x)\psi_0(y)$ and $\gamma_{s,\Psi_{0,0}}$ is the cross-correlation function defined as

$$\gamma_{s,\Psi_{0,0}}(x,y) = \int_{-\infty}^{\infty}\int_{-\infty}^{\infty} s(u,v)\Psi_{0,0}(u-x,v-y)\,du\,dv. \tag{31}$$

In the same way, we can project the analog image onto the dual approximation space

$$V_0^{\mathrm{H}} = \overline{\mathrm{Span}}\{\Psi_{0,0}^{\mathrm{H}}(x-k,y-l),(k,l)\in\mathbb{Z}^2\} \tag{32}$$

where $\Psi_{0,0}^{\mathrm{H}}(x,y) = \psi_0^{\mathrm{H}}(x)\psi_0^{\mathrm{H}}(y)$. We have then

$$P_{V_0^{\mathrm{H}}}(f(x,y)) = \sum_{k,l} c_{0,0,0}^{\mathrm{H}}[k,l]\;\Psi_{0,0}^{\mathrm{H}}(x-k,y-l)$$

where the dual approximation coefficients are given by

$$c_{0,0,0}^{\mathrm{H}}[k,l] = \sum_{p,q} f|p,q]\;\gamma_{s,\Psi_{0,0}^{\mathrm{H}}}(k-p,l-q). \tag{33}$$

Obviously, Eq. (30) and (33) can be interpreted as the use of two prefilters on the discrete image $(f[k,l])_{(k,l)\in\mathbb{Z}^2}$ before

the dual-tree decomposition. The frequency response of these filters are

$$F_1(\omega_x,\omega_y)=\sum_{p=-\infty}^{\infty}\sum_{q=-\infty}^{\infty}\widehat{s}(\omega_x+2p\pi,\omega_y+2q\pi)\,\widehat{\psi}_0^*(\omega_x+2p\pi)\widehat{\psi}_0^*(\omega_y+2q\pi) \quad (34)$$

$$F_2(\omega_x,\omega_y)=\sum_{p=-\infty}^{\infty}\sum_{q=-\infty}^{\infty}\widehat{s}(\omega_x+2p\pi,\omega_y+2q\pi)\,(\widehat{\psi}_0^{\mathrm{H}}(\omega_x+2p\pi))^*(\widehat{\psi}_0^{\mathrm{H}}(\omega_y+2q\pi))^*. \quad (35)$$

By using Eq. (22), it can be noticed that, when $\widehat{s}$ is compactly supported on $[-\pi,\pi[^2$, for all $(\omega_x,\omega_y)\in[-\pi,\pi[^2$,

$$F_2(\omega_x,\omega_y)=e^{\imath(d+1/2)(\omega_x+\omega_y)}F_1(\omega_x,\omega_y). \quad (36)$$

Different kinds of interpolation functions may be envisaged, in particular separable functions of the form $s(x,y)=\chi(x)\chi(y)$. The two prefilters are then separable with impulse responses $(\gamma_{\chi,\psi_0}(p)\gamma_{\chi,\psi_0}(q))_{(p,q)\in\mathbb{Z}^2}$ and $(\gamma_{\chi,\psi_0^{\mathrm{H}}}(p)\gamma_{\chi,\psi_0^{\mathrm{H}}}(q))_{(p,q)\in\mathbb{Z}^2}$, respectively. A natural choice for χ is the Shannon-Nyquist interpolation function, $\chi(t)=\mathrm{sinc}(\pi t)$, which allows the ideal digital-to-analog conversion of a band-limited signal. We have then, for $(\omega_x,\omega_y)\in[-\pi,\pi[^2$, $F_1(\omega_x,\omega_y)=\widehat{\psi}_0^*(\omega_x)\widehat{\psi}_0^*(\omega_y)$. Moreover, in the specific case when ψ_0 also corresponds to an ideal low-pass filter, that is $\psi_0(t)=\mathrm{sinc}(\pi t)$, the prefilter for the primal decomposition reduces to the identity ($F_1(\omega_x,\omega_y)=1$) whereas the prefilter for the dual decomposition is an half-integer shift with frequency response $F_2(\omega_x,\omega_y)=e^{\imath(d+1/2)(\omega_x+\omega_y)}$, for $(\omega_x,\omega_y)\in[-\pi,\pi[^2$.

2) M-band wavelet decompositions: The M-band multiresolution analysis of the first prefiltered image is performed, resulting in coefficients

$$c_{j,m,m'}[k,l]=\langle f(x,y),\frac{1}{M^j}\psi_m(\frac{x}{M^j}-k)\psi_{m'}(\frac{y}{M^j}-l)\rangle \quad (37)$$

where ($j\in\{1,\dots,J\}$ and $(m,m')\neq(0,0)$) or ($j=J$ and $m=m'=0$). In parallel, the dual decomposition of the second prefiltered image is computed, generating coefficients

$$c^{\mathrm{H}}_{j,m,m'}[k,l]=\langle f(x,y),\frac{1}{M^j}\psi^{\mathrm{H}}_m(\frac{x}{M^j}-k)\psi^{\mathrm{H}}_{m'}(\frac{y}{M^j}-l)\rangle. \quad (38)$$

3) Direction extraction in the different subbands: In order to better extract the local directions present in the image, it is useful to introduce linear combinations of the primal and dual subbands. To do so, we define the analytic wavelets as

$$\psi^a_m(t)=\frac{1}{\sqrt{2}}(\psi_m(t)+\imath\,\psi^{\mathrm{H}}_m(t)),\qquad m\in\{0,\dots,M-1\} \quad (39)$$

and the anti-analytic wavelets as

$$\psi^{\bar{a}}_m(t)=\frac{1}{\sqrt{2}}(\psi_m(t)-\imath\,\psi^{\mathrm{H}}_m(t)),\qquad m\in\{0,\dots,M-1\}. \quad (40)$$

Let us now calculate the tensor product of two analytic wavelets ψ^a_m and $\psi^a_{m'}$. More precisely, we are interested in the real part of this tensor product:

$$\Psi^a_{m,m'}(x,y)=\mathrm{Re}\{\psi^a_m(x)\psi^a_{m'}(y)\}=\frac{1}{2}\big(\psi_m(x)\psi_{m'}(y)-\psi^{\mathrm{H}}_m(x)\psi^{\mathrm{H}}_{m'}(y)\big). \quad (41)$$

For $(m,m')\in\{1,\dots,M-1\}^2$, using Eq. (4), the Fourier transform of this function is seen to be equal to

$$\widehat{\Psi}^a_{m,m'}(\omega_x,\omega_y)=\frac{1}{2}(1+\mathrm{sign}(\omega_x\,\omega_y))\widehat{\psi}_m(\omega_x)\widehat{\psi}_{m'}(\omega_y)=\begin{cases}\widehat{\psi}_m(\omega_x)\widehat{\psi}_{m'}(\omega_y) & \text{if } \mathrm{sign}(\omega_x)=\mathrm{sign}(\omega_y),\\ 0 & \text{if } \mathrm{sign}(\omega_x)\neq\mathrm{sign}(\omega_y).\end{cases} \quad (42)$$

As illustrated in Fig. 4, this function allows us to extract the "directions" falling in the first/third quarter of the frequency plane.

In the same way, the real part of the tensor product of an analytic wavelet and an anti-analytic one reads

$$\Psi^{\bar{a}}_{m,m'}(x,y)=\mathrm{Re}\{\psi^a_m(y)\psi^{\bar{a}}_{m'}(x)\} \quad (43)$$

and, for $(m,m')\in\{1,\dots,M-1\}^2$, its Fourier transform is

$$\widehat{\Psi}^{\bar{a}}_{m,m'}(\omega_x,\omega_y)=\begin{cases}\widehat{\psi}_m(\omega_x)\widehat{\psi}_{m'}(\omega_y) & \text{if } \mathrm{sign}(\omega_x)\neq\mathrm{sign}(\omega_y),\\ 0 & \text{if } \mathrm{sign}(\omega_x)=\mathrm{sign}(\omega_y).\end{cases} \quad (44)$$

Fig. 4 shows that these functions allow us to select frequency components which are localized in the second/fourth quarter of the frequency plane. This yields "opposite" directions to those obtained with $\Psi^a_{m,m'}$.

At a given resolution level j, for each subband (m,m') with $m\neq0$ and $m'\neq0$, the directional analysis is achieved by computing the coefficients

$$d_{j,m,m'}[k,l]=\sqrt{2}\langle f(x,y),\frac{1}{M^j}\Psi^{\bar{a}}_{m,m'}(\frac{x}{M^j}-k,\frac{y}{M^j}-l)\rangle \quad (45)$$

$$d^{\mathrm{H}}_{j,m,m'}[k,l]=\sqrt{2}\langle f(x,y),\frac{1}{M^j}\Psi^{a}_{m,m'}(\frac{x}{M^j}-k,\frac{y}{M^j}-l)\rangle. \quad (46)$$

According to Eqs. (39), (41), (40) and (43), we have for all $(m,m')\in\{1,\dots,M-1\}^2$,

$$d_{j,m,m'}[k,l]=\frac{1}{\sqrt{2}}(c_{j,m,m'}[k,l]+c^{\mathrm{H}}_{j,m,m'}[k,l]) \quad (47)$$

$$d^{\mathrm{H}}_{j,m,m'}[k,l]=\frac{1}{\sqrt{2}}(c_{j,m,m'}[k,l]-c^{\mathrm{H}}_{j,m,m'}[k,l]) \quad (48)$$

which amounts to applying a simple 2×2 isometry to the M-band wavelet coefficients. Note that Relations (42) and (44) are not valid for horizontal or vertical low-pass subbands such that $m=0$ or $m'=0$. The corresponding coefficients are left unchanged by setting $d_{j,m,m'}[k,l]=c_{j,m,m'}[k,l]$ and $d^{\mathrm{H}}_{j,m,m'}[k,l]=c^{\mathrm{H}}_{j,m,m'}[k,l]$.

To illustrate the improved directional analysis provided by the proposed decompositions, the basis functions used in a 3-band dual-tree structure are shown in Fig. 5.

B. Reconstruction

Let us denote by $\mathbf{f}\in\ell^2(\mathbb{Z}^2)$ the vector of image samples where $\ell^2(\mathbb{Z}^2)$ is the space of finite-energy 2D discrete fields. Besides, we denote by $\mathbf{c}$ the vector of coefficients generated by the primal M-band decomposition and by $\mathbf{c}^{\mathrm{H}}$ the vector of coefficients produced by the dual one. These vectors consist of M^2J-J+1 sequences each belonging to $\ell^2(\mathbb{Z}^2)$. The

linear combination of the subbands described in Section III-A.3 can be omitted in the subsequent analysis since we have seen that this post-processing reduces to a trivial 2×2 orthogonal transform. The global decomposition operator (including decomposition steps 1 and 2) is

$$\mathbf{D} \ : \mathbf{f} \mapsto \begin{pmatrix} \mathbf{c} \\ \mathbf{c}^{\mathrm{H}} \end{pmatrix} = \begin{pmatrix} \mathbf{D_1 f} \\ \mathbf{D_2 f} \end{pmatrix} \tag{49}$$

where $\mathbf{D_1} = \mathbf{U_1 F_1}$ and $\mathbf{D_2} = \mathbf{U_2 F_2}$, $\mathbf{F_1}$ and $\mathbf{F_2}$ being the prefiltering operations described in Section III-A.1 and $\mathbf{U_1}$ and $\mathbf{U_2}$ being the two considered orthogonal M-band wavelet decompositions. We have then the following result whose proof is provided in Appendix III:

Proposition 5: Provided that there exist positive constants A_s, B_s, C_s and A_{ψ_0} such that, for (almost) all $(\omega_x, \omega_y) \in [-\pi, \pi[^2$,

$$A_s \leq |\widehat{s}(\omega_x, \omega_y)| \leq B_s, \quad |\widehat{\psi}_0(\omega_x)| \geq A_{\psi_0} \tag{50}$$

$$\sum_{(p,q) \neq (0,0)} |\widehat{s}(\omega_x + 2p\pi, \omega_y + 2q\pi)|^2 \leq C_s < A_s^2 A_{\psi_0}^4 \tag{51}$$

$\mathbf{D}$ is a frame operator. The "dual" frame reconstruction operator is given by[1]

$$\mathbf{f} = (\mathbf{F_1}^{\dagger}\mathbf{F_1} + \mathbf{F_2}^{\dagger}\mathbf{F_2})^{-1} \ (\mathbf{F_1}^{\dagger}\mathbf{U_1}^{-1}\mathbf{c} + \mathbf{F_2}^{\dagger}\mathbf{U_2}^{-1}\mathbf{c^H}) \tag{52}$$

where $\mathbf{T}^{\dagger}$ designates the adjoint of an operator $\mathbf{T}$.

A particular case of interest is when $\{s(x-k, y-l), (k,l) \in \mathbb{Z}^2\}$ is an orthonormal family of $\mathrm{L}^2(\mathbb{R}^2)$. We then have $\sum_{p,q} |\widehat{s}(\omega_x + 2p\pi, \omega_y + 2q\pi)|^2 = 1$ and consequently we can choose $B_s = 1$. The lower bounds A_s and A_{ψ_0} prevent $\widehat{s}$ and $\widehat{\psi}_0$ from vanishing for low frequencies whereas Eq. (51) controls the amount of energy of $\widehat{s}$ out of the frequency band $[-1/2, 1/2[^2$. Note that the assumptions on s are obviously satisfied by the Shannon-Nyquist interpolation function.

Although other reconstructions of $\mathbf{f}$ from $(\mathbf{c}, \mathbf{c}^{\mathrm{H}})$ could be envisaged, Formula (52) minimizes the impact of possible errors in the computation of the wavelet coefficients. For example, these errors may arise in the estimation procedures when a denoising application is considered. Finally, it is worth pointing out that Eq. (52) is not difficult to implement since $\mathbf{U_1}^{-1}$ and $\mathbf{U_2}^{-1}$ are the inverse M-band wavelet transforms and $\mathbf{F_1}^{\dagger}$, $\mathbf{F_2}^{\dagger}$ and $(\mathbf{F_1}^{\dagger}\mathbf{F_1} + \mathbf{F_2}^{\dagger}\mathbf{F_2})^{-1}$ correspond to filtering with frequency responses $F_1^*(\omega_x, \omega_y)$, $F_2^*(\omega_x, \omega_y)$ and $(|F_1(\omega_x, \omega_y)|^2 + |F_2(\omega_x, \omega_y)|^2)^{-1}$, respectively.

IV. Implementation and design issues

A. M-band wavelet and filter bank families

In our experiments, the advantage of the dual-tree decomposition has been tested over several classical dyadic orthonormal wavelet bases. Since we are interested in its M-band generalization, several other M-band filter banks decompositions have been considered, including both M-band wavelets and lapped transforms (we refer to [23], [24] for more details on filter banks regularity):

- Primal wavelets with compact support: the first example consists in four finite impulse response (FIR) 16-tap filters (denoted as AC in [25]), generating regular, orthonormal and symmetric basis functions. The scaling function and the wavelets associated to the dual 4-band filter bank are represented in Fig. 6. We observe that the constructed dual wavelets possess regularity and satisfy the symmetry properties stated in Proposition 4. We also have constructed and tested dual wavelets from standard symmlets as well as a 4-channel modulated lapped transform [17].
- Primal wavelets without compact support: we have constructed M-band generalizations of Meyer's wavelets. The corresponding filters possess a good frequency selectivity. To implement these filters, we have used a method similar to that developed in [26]. Taking the same wavelet family with a different number of bands helps in providing fair assessment on the benefits of using more channels.

B. Frequency-domain implementation

Two solutions are possible to implement a wavelet decomposition: a time-domain or a frequency-domain approach. The first one is probably the most popular for classical wavelet decompositions when wavelets with compact support are used. Sometimes however, especially for wavelets having an infinite support (for instance orthonormal spline wavelets), a frequency-domain implementation is often preferable, taking advantage of FFT algorithms [27] (see also [28] for a thorough discussion of these problems). In particular, FFTs are used to compute Fractional Spline Wavelet Transform [29] and also to implement steerable pyramids [30]. In the case of dual-tree decompositions, we have noticed in Section II-D that, when the primal wavelets are compactly supported, the dual ones are not. If a time-domain implementation is chosen, it then becomes necessary to approximate the infinite impulse responses of the dual filter bank by finite sequences satisfying constraints related to the para-unitarity conditions, symmetry, number of vanishing moments, etc. The resulting optimal design problem may become involved and, for a good approximation of the ideal dual responses, it may happen that the obtained solutions only approximately satisfy the para-unitarity conditions which correspond to non-convex constraints. In spite of these difficulties, such an approach was followed in [31] which is approximate in the sense of the Hilbert transform and symmetry and in one of our previous work [1]. For the simulations in this paper, frequency-domain implementations have been adopted. They may provide better numerical solutions in the context of dual-tree decompositions. In this case, both convolutions and decimations/interpolations are performed in the frequency domain.

V. Application to denoising

The 2-band multidimensionnal dual-tree complex wavelet transform has already been proved to be useful in denoising problems, in particular for video processing [32] or satellite imaging [33]. In this part, we show that M-band dual-tree

[1]Here "dual" is meant in the sense of the frame theory [22] which is different from the sense given in the rest of the paper.

wavelet transforms also demonstrate good performances in image denoising and outperform existing methods such as those relying on classical M-band wavelet transforms ($M \geq 2$) or even 2-band dual-tree wavelet transforms. We will be mainly interested in applications involving images containing directional information and texture-like behavior such as seismic images.

A. Denoising problem

In this part, we will consider the estimation of an image s, corrupted by an additive zero-mean white Gaussian noise b with power spectrum density σ^2. The observed image $f(x,y)$ is therefore given by: $f(x,y) = s(x,y) + b(x,y)$. We will denote by $(b_{j,m,m'}[k,l])_{k,l}$ the coefficients resulting from a 2D M-band wavelet decomposition of the noise in a given subband (j,m,m'). The associated wavelet coefficients of the dual decomposition are denoted by $(b^{\mathrm{H}}_{j,m,m'}[k,l])_{k,l}$. These sequences are white zero-mean Gaussian with variance σ^2. Besides, we have for all $(k,l) \in \mathbb{Z}^2$,

$$\begin{aligned}&\mathsf{E}\{b_{j,m,m'}[k,l]b^{\mathrm{H}}_{j,m,m'}[k,l]\} = \\ &\int_{\mathbb{R}^4} \mathsf{E}\{b(x,y)b(x',y')\}\frac{1}{M^j}\psi_m(\frac{x}{M^j}-k)\psi_{m'}(\frac{y}{M^j}-l) \\ &\qquad \frac{1}{M^j}\psi^{\mathrm{H}}_m(\frac{x'}{M^j}-k)\psi^{\mathrm{H}}_{m'}(\frac{y'}{M^j}-l)\; dxdydx'dy' \quad (53)\end{aligned}$$

where $\mathsf{E}\{b(x,y)b(x',y')\} = \sigma^2\ \delta(x-x')\delta(y-y')$ (δ is the Dirac distribution). After some straightforward calculations when $m \neq 0$ or $m' \neq 0$, this yields

$$\mathsf{E}\{b_{j,m,m'}[k,l]b^{\mathrm{H}}_{j,m,m'}[k,l]\} = 0. \quad (54)$$

It is deduced that, when $m \neq 0$ or $m' \neq 0$, the Gaussian vector $(b_{j,m,m'}[k,l] \quad b^{\mathrm{H}}_{j,m,m'}[k,l])^T$ has independent components.

The variance of the noise may be unknown. In such a case, we use a robust estimator $\hat{\sigma}$ of σ which is computed from the wavelets coefficients at scale $j = 1$ in a high-pass subband (see [3, p. 447]):

$$\hat{\sigma} = \frac{1}{0.6745}\ \mathrm{median}[(|c_{1,M-1,M-1}[k,l]|)_{(k,l)}]. \quad (55)$$

B. Thresholding

Various thresholding techniques have been applied on the wavelet coefficients of the observed image f. Although many choices of estimators can be envisaged, we have studied the following ones:

- Visushrink (see [34]) defined by the "universal" hard threshold $T = \sigma\ \sqrt{2\ \ln(N)}$, N being the number of pixels of the original image.
- Hybrid SUREshrink [35], [36]. This subband-adaptive threshold technique relies on Stein's Unbiased Risk Estimate and uses a soft thresholding. As a result, if the signal to noise ratio is very small, the SURE estimate may become unreliable. If such a situation is detected, a universal threshold is used.
- Cai and Silverman estimator [37]. This block thresholding approach exploits correlations between neighboring coefficients. In our work, we use a variant of the NeighBlock method.
- Bivariate Shrinkage [38]. This method exploits the inter-scale dependencies i.e. relations between the coefficients and their parents.

C. Mesures of performance

Let N be the number of points in the observed image f, σ_s the standard deviation of s. We define two signal-to-noise ratios, denoted by SNR, as:

$$\begin{aligned}\mathrm{SNR}_{\text{initial}} &= 10\ \log_{10}\left(\frac{\sigma_s^2\ N}{\|s-f\|^2}\right) \\ \mathrm{SNR}_{\text{final}} &= 10\ \log_{10}\left(\frac{\sigma_s^2\ N}{\|s-\hat{s}\|^2}\right) \quad (56)\end{aligned}$$

where $\hat{s}$ is the estimated image.

Visual comparisons are provided as well, since SNR does not always faithfully accounts for image quality, especially in highly structured areas (textures, edges,...)

D. Experimental results

Tests have been carried out on a variety of images corrupted by an additive zero-mean white Gaussian noise. We have considered two possible situations : first, when the noise variance is known and second, when it is not. In the latter case, the noise variance is estimated with the robust median estimator as defined in Eq. (55). The noisy image is decomposed via an M-band DWT or an M-band Dual-Tree Transform (DTT) in the 2, 3 and 4-band cases. For each decomposition, the number of decomposition levels is fixed so as to get approximation images having roughly the same size at the coarsest resolution. This means that 2-band decompositions are carried out over 4 resolution, whereas 3 or 4-band decompositions are performed over 2 resolution levels. Under these conditions, the computational costs of the different M-band decompositions are comparable. Different wavelet families have been tested, the provided results corresponding to the use of Meyer's wavelets [26]. For various noise levels, the values of the SNR's are obtained from a Monte Carlo study over ten noise realizations.

Since we address more specifically the ability of the M-band DTT to preserve features in specific directions, comparisons are made on the following three images containing rich directional contents: a high frequency textured image, the standard Barbara image and a set of 2D seismic data with oriented patterns.

- We have first applied our method on a 512×512 directional texture image (Straw D15 image from the Brodatz album) corrupted by an additive zero-mean white Gaussian noise.
  The obtained SNR's (in dB) for three different initial noise levels are listed in Tab. I. We observe for this image that, by increasing the number of bands M, the denoising results are improved in almost all cases for the DWT (sometimes only marginally) and significantly in almost

all cases for the DTT. Furthermore, the DTT clearly leads to an improvement of the denoising performance compared with the DWT, whatever the initial SNR or the threshold selection method is. We remark that the more dramatic improvement over DWT is observed for Visushrink, which does not perform very well compared with SURE, NeighBlock or Bivariate. Results are also relatively consistent between the top (noise variance known) and the bottom of the table (noise variance unknown), which is important in real applications where noise statistics often have to be estimated from the data. Fig. 7 also illustrates that, compared with other decompositions, the DTT with $M = 4$ leads to sharper visual results and reduced artifacts. It can be seen from the bottom left corner that a 4-band DTT (Fig. 7d) better preserves the thin lines that are often blurred or merged in the other cropped images.

- Second, we have performed the same denoising tests on the 512×512 8-bit Barbara image. The obtained SNR's (in dB) are listed in Tab. II.
  For this image, we observe that, by increasing the number of bands M, the denoising results are improved in almost all cases both for the DWT and the DTT. Furthermore, the DTT clearly outperforms the DWT, as in the textured image case.
  Fig. 8 represents a zoom on a leg with a regular texture. This illustrates that, compared with other decompositions, the 4-band DTT leads to better visual results. Fig. 8a corresponding to the 2-band DWT is strongly blurred. Details are better preserved in the 4-band decomposition (Fig. 8b), but it clearly appears that the texture with an apparent angle of $\pi/4$ is heavily corrupted by patterns in the opposite direction, due to the mixing in the "diagonal" subband. Although Fig. 8c remains blurry, there is much less directional mixture in both DTT decompositions.
- Finally, we have tested our method on a 512×512 seismic image displayed in Fig. 9a. The data exhibits mostly horizontal structures as well as other directions which are important to the geophysicist for the underground analysis.
  Similarly to previous cases, the seismic image is corrupted by an additive white Gaussian noise. The obtained denoising results are listed in Tab. III.
  We observe that in most of the cases, denoising improves objectively with the increase of the number of bands M, with DWT and DTT as well. Again, the best results are obtained with both dual-tree and a 4-band wavelet, but the gain over traditional DWT is sometimes smaller than in the previous example, for instance for NeighBlock shrinkage. It should be noted that the original image is not noise-free in general. SNR measures are therefore more difficult to interpret. The existence of prior noise may explain the relatively weaker SNR increase between DWT and DTT, since denoising may attempt to remove both the added and the original noise, and thus the denoised image strays away from the original noisy data.
  Fig. 9b represents the original data corrupted with a -2 dB additive noise. Figs. 9c-d display the results with 2- and 4-band DTT respectively. Some of the oblique features (e.g. on the top-right corner) that are almost hidden in the noisy image become apparent in both the 2- and the 4-band DTT. We observe for this image that denoising results are more satisfactory with a 4-band than with a 2-band DTT: the 2-band denoising image possesses larger blurred areas, especially in weakly energetic zones. Careful examination also indicates a reduced presence of mosquito effects in the 4-band case.

We have experimented the DTT denoising algorithm on other image sets. Dual-tree M-band structures with $M > 2$ generally outperform existing wavelet decompositions in terms of SNR. We shall remark that visual improvement is not always perceptible in image areas with weak directionality.

E. Basis choice

The previous section focused on the comparison between DWT and DTT with M-band Meyer wavelets, for different images, noise levels and threshold selection methods. Choosing a single wavelet family allowed us to provide a relatively fair comparison concerning the choice of the different aforementioned characteristics but it also appears interesting to evaluate the influence of the decomposition filters. Amongst a variety of choices, we have tested 2-band symmlets (with length 8), the basic 4-band Modulated Lapped Transform (MLT, see [17]) and finally, Alkin and Caglar 4-band filter bank [25]. The results concerning Meyer's wavelets can be found in previous tables.

The results reported in Tab. IV show the superiority of the M-band DTT (with $M > 1$) over M-band DWT or 2-band DTT, in particular when the popular symmlets are employed. There is however no family which always leads to the best results. We remark indeed that DT MLT or AC DTT may lead to slightly improved results compared with Meyer DTT, but the best choice often depends on the image.

VI. Conclusion

Motivated by applications where directional selectivity is of main interest, we have proposed an extension of existing works on Hilbert transform pairs of dyadic orthonormal wavelets to the M-band case. In this context, we have pointed out that, when several wavelet decompositions are performed in parallel, special care should be taken concerning their implementation, by designing appropriate pre- and post-processing stages. Since the decomposition is redundant, an optimal reconstruction has also been proposed.

By taking advantage of the Hilbert pair conditions and M-band features which offer additional degrees of freedom, this new transform has been applied to image denoising. Various simulations have allowed us to conclude that dual-tree decompositions with more than two bands generally outperform discrete orthonormal wavelet decompositions and dyadic dual-tree representations.

Encouraged by these results, we will consider further improvements with other filter bank designs, including regularity, as well as applications of dual-tree M-band wavelets to other signal and image processing tasks, especially in seismics.

APPENDIX I
PROOF OF PROPOSITION 2:

Assuming that $\tilde{\theta}_0$ verifies the linearity relation (18) and using the fact that it is an odd function, we find that

$$\forall\, \omega \in]-2\pi, 2\pi[,$$
$$\beta(\omega) = \sum_{i=1}^{\infty} \tilde{\theta}_0(\frac{\omega}{M^i}) = \gamma \frac{\omega}{M} \sum_{i=0}^{\infty} \frac{1}{M^i} = \frac{\gamma\omega}{M-1}. \quad (57)$$

We deduce from Eq. (13) that, for all $m \in \{1, \ldots, M-1\}$,

$$\forall\, \omega \in]-\frac{2\pi}{M}, \frac{2\pi}{M}[$$
$$\tilde{\alpha}_{0,m}(\omega) = \frac{\pi}{2}\text{sign}(\omega) - \frac{\gamma\omega M}{M-1} \pmod{2\pi}. \quad (58)$$

Furthermore, according to Condition $(\mathsf{P}_{0,m})$,

$$\forall\, \omega \in]-\frac{2\pi}{M}, 0] \qquad \tilde{\alpha}_{0,m}(\omega + \frac{2\pi}{M}) = \tilde{\alpha}_{0,m}(\omega) \pmod{2\pi}. \quad (59)$$

This allows us to claim that there exists $d \in \mathbb{Z}$ such that

$$\gamma = (d + \frac{1}{2})(M-1). \quad (60)$$

This leads to the expression of $\tilde{\alpha}_{0,m}$ in Eq. (19). As $\tilde{\alpha}_{0,m}$ is a $2\pi/M$-periodic function, it is fully defined by its expression on $[0, \frac{2\pi}{M}[$. In contrast, we have to determine the expression of $\tilde{\theta}_0$ outside the interval $]-\frac{2\pi}{M}, \frac{2\pi}{M}[$. Using Eqs (13) and (17), we obtain, for all $m \in \{0, \ldots, M-1\}$,

$$\tilde{\alpha}_{0,m}(\frac{\omega}{M}) + \tilde{\theta}_0(\frac{\omega}{M}) + \beta(\frac{\omega}{M}) = \frac{\pi}{2}\text{sign}(\omega) \pmod{2\pi}$$
$$\iff \tilde{\theta}_0(\omega) = \frac{\pi}{2}\text{sign}(\omega) - \beta(\omega) - \tilde{\alpha}_{0,m}(\omega) \pmod{2\pi}. \quad (61)$$

Consider now the interval $[p\frac{2\pi}{M}, (p+1)\frac{2\pi}{M}[$ where $p \in \left\{1, \ldots, \left\lceil \frac{M}{2} \right\rceil - 1\right\}$. As $[p\frac{2\pi}{M}, (p+1)\frac{2\pi}{M}[\subset [0, 2\pi[$, Eq. (57) yields

$$\forall \omega \in [p\frac{2\pi}{M}, (p+1)\frac{2\pi}{M}[, \qquad \beta(\omega) = (d + \frac{1}{2})\omega. \quad (62)$$

Using Eq. (61) and the $2\pi/M$-periodicity of $\tilde{\alpha}_{0,m}$, we deduce that

$$\forall \omega \in [p\frac{2\pi}{M}, (p+1)\frac{2\pi}{M}[,$$
$$\tilde{\theta}_0(\omega) = \frac{\pi}{2} - (d + \frac{1}{2})\omega - \tilde{\alpha}_{0,m}(\omega - \frac{2\pi}{M}p) \pmod{2\pi}. \quad (63)$$

Combining this result with Eq. (19) leads to Eq. (20). As a consequence of the antisymmetry of the phase of a real filter, a similar expression is obtained for $p \in \left\{\left\lceil \frac{M}{2} \right\rceil, \ldots, M-1\right\}$:

$$\forall \omega \in \left]p\frac{2\pi}{M}, (p+1)\frac{2\pi}{M}\right],$$
$$\tilde{\theta}_0(\omega) = (d + \frac{1}{2})(M-1)\,\omega - p\pi \pmod{2\pi}. \quad (64)$$

In summary, under the considered assumptions, we have seen that, if there exists a solution to Eq. (13), it is given by Eqs. (19) and (20). Conversely, we will now prove that any filters satisfying Eqs. (19) and (20) are solutions to Eq. (13). More precisely, we will proceed by induction to show that

$$\forall k \in \mathbb{N}, \forall \omega \in]2k\pi, 2(k+1)\pi[,$$
$$\beta(\omega) = (d + \frac{1}{2})\omega - k\pi \pmod{2\pi} \quad (65)$$
$$\text{and } \tilde{\alpha}_{0,m}(\frac{\omega}{M}) + \beta(\omega) = \frac{\pi}{2} \pmod{2\pi}. \quad (66)$$

- It is readily checked that the properties (65)-(66) are satisfied for $k = 0$.
- Assuming that the properties hold true up to the index $k-1 \geq 0$, we will demonstrate it remains valid at index k.
  We can write $k = Mp+q$ with $p \in \mathbb{N}$ and $q \in \{0, ..., M-1\}$ and, consequently,

$$\omega \in]2k\pi, 2(k+1)\pi[\iff \quad (67)$$
$$\frac{\omega}{M} \in]2(p + \frac{q}{M})\pi, 2(p + \frac{q+1}{M})\pi[\subset]2p\pi, 2(p+1)\pi[.$$

  Since $p < k$, according to the induction hypothesis, we have $\forall \omega \in]2k\pi, 2(k+1)\pi[$,

$$\beta(\frac{\omega}{M}) = (d + \frac{1}{2})\frac{\omega}{M} - p\pi \pmod{2\pi}. \quad (68)$$

  Moreover, the 2π-periodicity of $\tilde{\theta}_0$ allows us to write:

$$\tilde{\theta}_0(\frac{\omega}{M}) = \tilde{\theta}_0(\frac{\omega}{M} - 2p\pi). \quad (69)$$

  As $\omega/M - 2p\pi \in]2q\frac{\pi}{M}, 2(q+1)\frac{\pi}{M}[$, Eqs. (20) and (64) lead to

$$\tilde{\theta}_0(\frac{\omega}{M}) = \frac{M-1}{M}(d + \frac{1}{2})\omega \quad (70)$$
$$- \big((2d+1)(M-1)p + q\big)\pi \pmod{2\pi}$$
$$= \frac{M-1}{M}(d + \frac{1}{2})\omega - (k-p)\pi \pmod{2\pi}.$$

  Combining Eqs. (17), (68) and (70), Eq. (65) is obtained. By invoking the $2\pi/M$-periodicity of $\tilde{\alpha}_{0,m}$, the second part of the property is proved in the similar way. Indeed, for $\omega \in]2k\pi, 2(k+1)\pi[$, we have:

$$\tilde{\alpha}_{0,m}(\frac{\omega}{M}) = \tilde{\alpha}_{0,m}(\frac{\omega}{M} - 2(p + \frac{q}{M})\pi) \quad (71)$$

  which, using Eq. (19), leads to

$$\tilde{\alpha}_{0,m}(\frac{\omega}{M}) = \frac{\pi}{2} - (d + \frac{1}{2})M(\frac{\omega}{M} - 2(p + \frac{q}{M})\pi)$$
$$= \frac{\pi}{2} - (d + \frac{1}{2})\omega + k\pi \pmod{2\pi}. \quad (72)$$

  Then, summing Eq. (65) and the above expression results in Eq. (66).

In conclusion, we have proved by induction that Eq. (66) holds for almost all $\omega > 0$. The function $\tilde{\theta}_0$ (and thus β) being odd as well as $\tilde{\alpha}_{0,m}$, we deduce that Eq. (13) is satisfied almost everywhere. This ends the proof of Proposition 2.

APPENDIX II
PROOF OF PROPOSITION 4:

Assuming h_0 is symmetric w.r.t. k_0, we have

$$\forall k \in \mathbb{Z}, \qquad h_0[2k_0 - k] = h_0[k] \tag{73}$$
$$\Longleftrightarrow e^{-2\imath k_0 \omega} H_0^*(\omega) = H_0(\omega). \tag{74}$$

Thanks to Eq. (10), this may be rewritten as

$$e^{-2\imath k_0 \omega} e^{-2\imath \theta_0(\omega)} G_0^*(\omega) = G_0(\omega). \tag{75}$$

According to Eq. (20),

$$2\theta_0(\omega) = (2d+1)(M-1)\omega \pmod{2\pi}. \tag{76}$$

which leads to

$$\forall k \in \mathbb{Z}, \qquad g_0[2k_0 + (2d+1)(M-1) - k] = g_0[k]. \tag{77}$$

This shows that g_0 is symmetric w.r.t. $k_0 + (d+\frac{1}{2})(M-1)$.

In the same way, for any $m \in \{1, ..., M-1\}$, the symmetry/antisymmetry property:

$$\forall k \in \mathbb{Z}, \qquad h_m[2k_m - k] = \pm h_m[k] \tag{78}$$

combined with Eq. (21), results in:

$$\forall k \in \mathbb{Z}, \qquad g_m[2k_m - 2d - 1 - k] = \mp g_m[k]. \tag{79}$$

APPENDIX III
PROOF OF PROPOSITION 5:

We denote by $\|.\|$ the norms of the underlying Hilbert spaces. We have then, for all $\mathbf{f} \in \ell^2(\mathbb{Z}^2)$,

$$\|\mathbf{D}\mathbf{f}\|^2 = \|\mathbf{D_1}\mathbf{f}\|^2 + \|\mathbf{D_2}\mathbf{f}\|^2. \tag{80}$$

Let us next focus on the first term on the right-hand side of this equation. As $\mathbf{U_1}$ is unitary, we have

$$\begin{aligned}\|\mathbf{D_1}\mathbf{f}\|^2 &= \|\mathbf{F_1}\mathbf{f}\|^2 \qquad (81)\\ &= \frac{1}{(2\pi)^2}\int_{-\pi}^{\pi}\int_{-\pi}^{\pi} |F_1(\omega_x,\omega_y)\widehat{f}(\omega_x,\omega_y)|^2\, d\omega_x\, d\omega_y.\end{aligned}$$

In Equation (34), we upper bound the magnitude of the sums by the sum of magnitudes. Invoking the Cauchy-Schwarz inequality, the modulus of the frequency response of the first prefilter satisfies the following inequality:

$$\begin{aligned}|F_1(\omega_x,\omega_y)| &\le \Big(\sum_{p,q} |\widehat{s}(\omega_x+2p\pi,\omega_y+2q\pi)|^2\Big)^{1/2}\\ &\Big(\sum_p |\widehat{\psi}_0(\omega_x+2p\pi)|^2\Big)^{1/2}\Big(\sum_q |\widehat{\psi}_0(\omega_y+2q\pi)|^2\Big)^{1/2}. \qquad (82)\end{aligned}$$

As $\{\psi_0(t-k), k \in \mathbb{Z}\}$ is an orthonormal family of $\mathrm{L}^2(\mathbb{R})$, $\sum_{p=-\infty}^{\infty} |\widehat{\psi}_0(\omega_x+2p\pi)|^2 = 1$. Under the Assumptions (50) and (51), we deduce that

$$|F_1(\omega_x,\omega_y)| \le \sqrt{B_s^2 + C_s}. \tag{83}$$

Besides, the frequency magnitude of the first prefilter can be lower bounded as follows:

$$\begin{aligned}&|F_1(\omega_x,\omega_y)| \ge |\widehat{s}(\omega_x,\omega_y)\widehat{\psi}_0(\omega_x)\widehat{\psi}_0(\omega_y)|\\ &- \sum_{\substack{(p,q)\\ \neq(0,0)}} |\widehat{s}(\omega_x+2p\pi,\omega_y+2q\pi)\widehat{\psi}_0(\omega_x+2p\pi)\widehat{\psi}_0(\omega_y+2q\pi)|.\end{aligned} \tag{84}$$

The latter summation can be upper bounded as we did for $|F_1(\omega_x,\omega_y)|$, which combined with the assumptions (50) and (51), yields:

$$|F_1(\omega_x,\omega_y)| \ge A_s A_{\psi_0}^2 - \sqrt{C_s}. \tag{85}$$

From Eqs. (81), (83) and (85), we conclude that

$$(A_s A_{\psi_0}^2 - \sqrt{C_s})\|\mathbf{f}\| \le \|\mathbf{D_1}\mathbf{f}\| \le \sqrt{B_s^2 + C_s}\|\mathbf{f}\|. \tag{86}$$

Now, using Eq. (35) and invoking the same arguments as previously lead to

$$(A_s A_{\psi_0}^2 - \sqrt{C_s})\|\mathbf{f}\| \le \|\mathbf{D_2}\mathbf{f}\| \le \sqrt{B_s^2 + C_s}\|\mathbf{f}\|. \tag{87}$$

Combining Eqs. (86) and (87) allows us to conclude that

$$\sqrt{2}(A_s A_{\psi_0}^2 - \sqrt{C_s})\|\mathbf{f}\| \le \|\mathbf{D}\mathbf{f}\| \le \sqrt{2(B_s^2 + C_s)}\|\mathbf{f}\|. \tag{88}$$

As we have assumed in Eq. (51) that $A_s A_{\psi_0}^2 - \sqrt{C_s} > 0$, this means that $\mathbf{D}$ is a frame operator. Note that, when ideal low-pass filters are used for s and ψ_0 (that is $s(x,y) = \psi_0(x)\psi_0(y)$ with $\psi_0(t) = \mathrm{sinc}(\pi t)$), we have $|F_1(\omega_x,\omega_y)| = |F_2(\omega_x,\omega_y)| = 1$, and thus, $\|\mathbf{D_1}\mathbf{f}\| = \|\mathbf{D_2}\mathbf{f}\| = \|\mathbf{f}\|$. Therefore, in this ideal case, $\mathbf{D}$ is a tight frame operator with bound 2.

To determine the "dual" frame reconstruction operator, we have to calculate the pseudo-inverse of $\mathbf{D}$ which is defined by $\mathbf{D}^\sharp = (\mathbf{D}^\dagger\mathbf{D})^{-1}\mathbf{D}^\dagger$. In our case, the adjoint of $\mathbf{D}$ is

$$\mathbf{D}^\dagger = (\mathbf{D_1}^\dagger \quad \mathbf{D_2}^\dagger) = (\mathbf{F_1}^\dagger\mathbf{U_1}^\dagger \quad \mathbf{F_2}^\dagger\mathbf{U_2}^\dagger). \tag{89}$$

Hence, by virtue of the unitarity of $\mathbf{U_1}$ and $\mathbf{U_2}$, we obtain $\mathbf{D}^\dagger\mathbf{D} = \mathbf{F_1}^\dagger\mathbf{F_1} + \mathbf{F_2}^\dagger\mathbf{F_2}$
and, finally,

$$\mathbf{D}^\sharp = (\mathbf{F_1}^\dagger\mathbf{F_1} + \mathbf{F_2}^\dagger\mathbf{F_2})^{-1}\,(\mathbf{F_1}^\dagger\mathbf{U_1}^{-1} \quad \mathbf{F_2}^\dagger\mathbf{U_2}^{-1}). \tag{90}$$

REFERENCES

[1] C. Chaux, L. Duval, and J.-C. Pesquet, "Hilbert pairs of M-band orthonormal wavelet bases," in *Proc. Eur. Sig. and Image Proc. Conference*, Vienna, Austria, September 6-10, 2004, pp. 1187–1190.

[2] ——, "$2D$ dual-tree M-band wavelet decomposition," in *Proc. Int. Conf. on Acoust., Speech and Sig. Proc.*, Philadelphia, USA, March 18-23, 2005.

[3] S. Mallat, *A wavelet tour of signal processing*. Academic Press, 1998.

[4] G. P. Nason and B. W. Silverman, *The stationary wavelet transform and some statistical applications*, pp. 281–300.

[5] J.-C. Pesquet, H. Krim, and H. Carfantan, "Time invariant orthonormal representations," *IEEE Trans. on Signal Proc.*, vol. 44, no. 8, pp. 1964–1970, 1996.

[6] X.-P. Zhang, M. Desai, and Y.-N. Peng, "Orthogonal complex filter banks and wavelets: some properties and design," *IEEE Trans. on Signal Proc.*, vol. 47, no. 4, pp. 1039–1048, Apr. 1999.

[7] E. P. Simoncelli, W. T. Freeman, E. H. Adelson, and D. J. Heeger, "Shiftable multi-scale transforms," *IEEE Trans. on Inform. Theory*, vol. 38, no. 2, pp. 587–607, March 1992, special Issue on Wavelets.

[8] N. Kingsbury, "Complex wavelets for shift invariant analysis and filtering of signals," *J. of Appl. and Comp. Harm. Analysis*, vol. 10, no. 3, pp. 234–253, May 2001.

[9] P. Abry and P. Flandrin, "Multiresolution transient detection," in *Proc. Int. Symp. on Time-Freq. and Time-Scale Analysis*, Philadelphia, USA, October 1994, pp. 225–228.

[10] I. W. Selesnick, "Hilbert transform pairs of wavelet bases," *Signal Processing Letters*, vol. 8, no. 6, pp. 170–173, Jun. 2001.

[11] ——, "The double-density dual-tree DWT," *IEEE Trans. on Signal Proc.*, vol. 52, no. 5, pp. 1304–1314, May 2004.

[12] R. A. Gopinath, "The phaselet transform — an integral redundancy nearly shift-invariant wavelet transform," *IEEE Trans. on Signal Proc.*, pp. 1792– 1805, Jul. 2003.

[13] F. Fernandes, M. Wakin, and R. Baraniuk, "Non-redundant, linear-phase, semi-orthogonal, directional complex wavelets," in *Proc. Int. Conf. on Acoust., Speech and Sig. Proc.*, Montral, Canada, May 17-21, 2004.

[14] R. van Spaendonck, T. Blu, R. Baraniuk, and M. Vetterli, "Orthogonal Hilbert transform filter banks and wavelets," in *Proc. Int. Conf. on Acoust., Speech and Sig. Proc.*, Hong Kong, China, April 6-10, 2003.

[15] S. C. Olhede and A. T. Walden, "Analytic wavelet thresholding," Imperial College," TR-03-01, 2003.

[16] W. Chan, H. Choi, and R. Baraniuk, "Directional hypercomplex wavelets for multidimensional signal analysis and processing," in *Proc. Int. Conf. on Acoust., Speech and Sig. Proc.*, May 2004.

[17] H. S. Malvar, *Signal Processing with Lapped Transforms.* Artech House, 1992.

[18] P. Steffen, P. N. Heller, R. A. Gopinath, and C. S. Burrus, "Theory of regular M-band wavelet bases," *IEEE Trans. on Signal Proc.*, vol. 41, no. 12, pp. 3497–3511, Dec. 1993.

[19] T. D. Tran, R. L. de Queiroz, and T. Q. Nguyen, "Linear phase perfect reconstruction filter bank: lattice structure, design, and application in image coding," *IEEE Trans. on Signal Proc.*, vol. 48, pp. 133–147, Jan. 2000.

[20] H. Ozkaramanli and R. Yu, "On the phase condition and its solution for hilbert transform pairs of wavelet bases," *IEEE Trans. on Signal Proc.*, 2003.

[21] D. Tay and M. Palaniswami, "Solution to the orthogonal M-channel bandlimited wavelet construction proposition," in *Proc. Int. Conf. on Acoust., Speech and Sig. Proc.*, Montreal, Quebec, Canada, May 17-21, 2004.

[22] I. Daubechies, *Ten Lectures on wavelets*, ser. CBMS Lecture Series. SIAM, 1992.

[23] S. Oraintara, T. D. Tran, P. N. Heller, and T. Q. Nguyen, "Lattice structure for regular paraunitary linear-phase filterbanks and M-band orthogonal symmetric wavelets," *IEEE Trans. on Signal Proc.*, vol. 49, no. 11, pp. 2659–2672, 2001.

[24] Y.-J. Chen and K. Amaratunga, "M-channel lifting factorization of perfect reconstruction filter banks and reversible M-band wavelet transforms," *IEEE Trans. on CAS II*, Dec. 2003.

[25] O. Alkin and H. Caglar, "Design of efficient M-band coders with linear-phase and perfect-reconstruction properties," *IEEE Trans. on Signal Proc.*, vol. 43, no. 9, pp. 1579–1590, 1995.

[26] B. Tennant and R. M. Rao, "Solution to the orthogonal M-channel bandlimited wavelet construction proposition," in *Proc. Int. Conf. on Acoust., Speech and Sig. Proc.*, Hong Kong, China, April 6-10, 2003.

[27] F. Nicolier, F. Truchetet, and O. Laligant, "Discrete wavelet transform implementation in fourier domain for multidimensional signal," *Journal of Electronic Imaging*, vol. vol. 11 (3), no. 3, pp. pp. 338–346, July 2002.

[28] O. Rioul and P. Duhamel, "Fast algorithms for discrete and continuous wavelet transforms," *IEEE Trans. on Inform. Theory*, vol. 38, pp. 569–586, Mar. 1992.

[29] T. Blu and M. Unser, "The fractional spline wavelet transform: Definition and implementation," in *Proc. Int. Conf. on Acoust., Speech and Sig. Proc.*, vol. I, Istanbul, Turkey, June 5-9, 2000, pp. 512–515.

[30] E. P. Simoncelli and W. T. Freeman, "The steerable pyramid : A flexible architecture for multiscale derivative computation," in *Proc. Int. Conf. on Image Processing*, vol. III, Washington, DC., Oct. 1995, pp. 444–447.

[31] I. W. Selesnick, "The design of approximate Hilbert transform pairs of wavelet bases," *IEEE Trans. on Signal Proc.*, vol. 50, no. 5, pp. 1144–1152, May 2002.

[32] I. Selesnick and K. Y. Li, "Video denoising using 2D and 3D dual-tree complex wavelet transforms," in *Wavelet Applications in Signal and Image Processing X (Proc. SPIE 5207)*, 2003.

[33] A. Jalobeanu, L. Blanc-Féraud, and J. Zerubia, "Satellite image debblurring using complex wavelet packets," *International Journal of Computer Vision*, vol. vol. 51, no. 3, pp. pp. 205–217, 2003.

[34] D. L. Donoho and I. M. Johnstone, "Ideal spatial adaptation by wavelet shrinkage," *Biometrika*, vol. 81, pp. 425–455, Sep. 1994.

[35] ——, "Adapting to unknown smoothness via wavelet shrinkage," *Journal of the American Statistical Association*, vol. 90, pp. 1200–1224, December 1995.

[36] H. Krim, D. Tucker, S. Mallat, and D. Donoho, "On denoising and best signal representation," *IEEE Transactions on Information Theory*, vol. 45, no. 7, pp. 2225–2238, Nov. 1999.

[37] T. T. Cai and B. W. Silverman, "Incorporating information on neighboring coefficients into wavelet estimation," *Sankhya*, vol. 63, pp. 127–148, 2001.

[38] L. Sendur and I. W. Selesnick, "Bivariate shrinkage with local variance estimation," *Signal Processing Letters*, vol. 9, no. 12, pp. 438–441, Dec. 2002.

LIST OF FIGURES

LIST OF TABLES

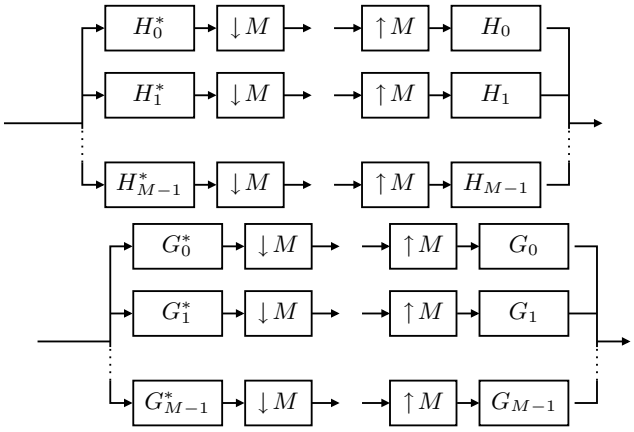

Fig. 1. A pair of analysis/synthesis M-band para-unitary filter banks.

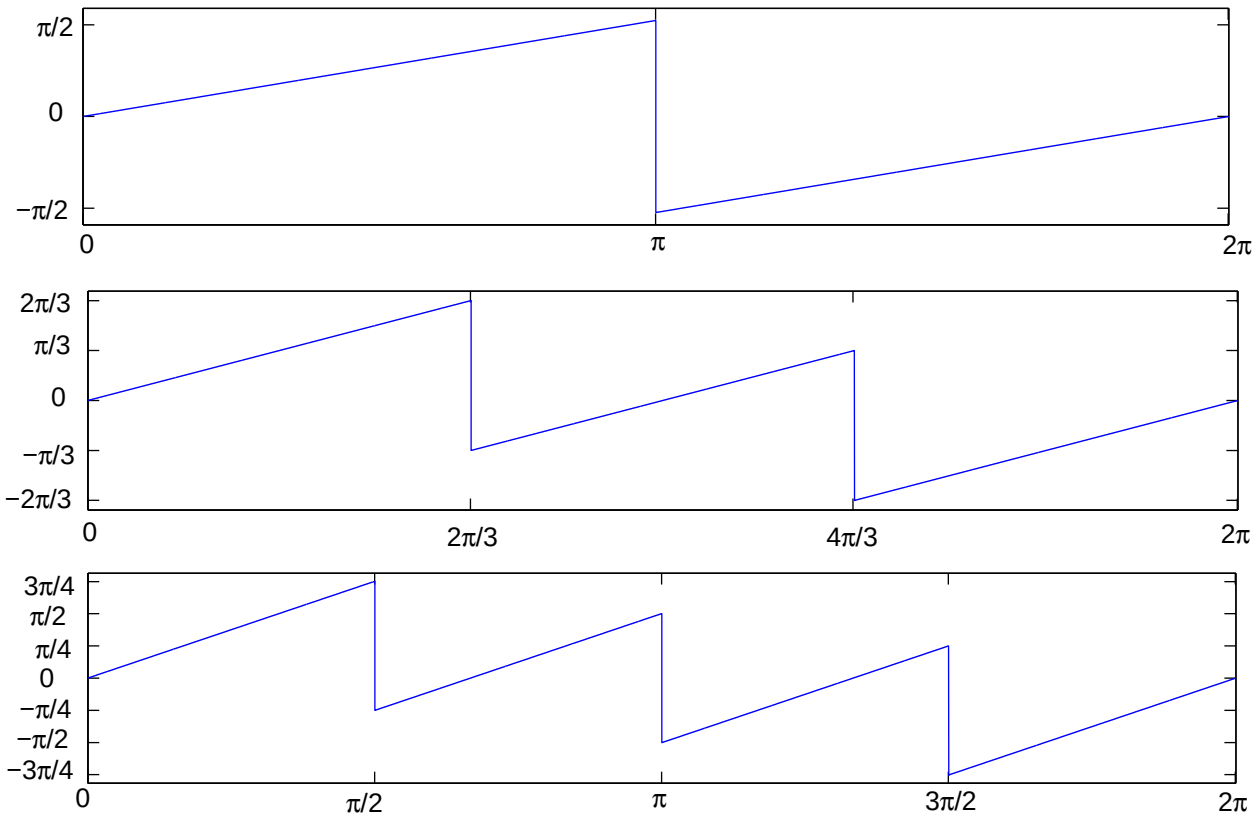

Fig. 2. Variations of $\tilde{\theta}_0(\omega)$ w.r.t. ω, for different numbers of channels: $M = 2$ (top), $M = 3$ (middle) and $M = 4$ (bottom).

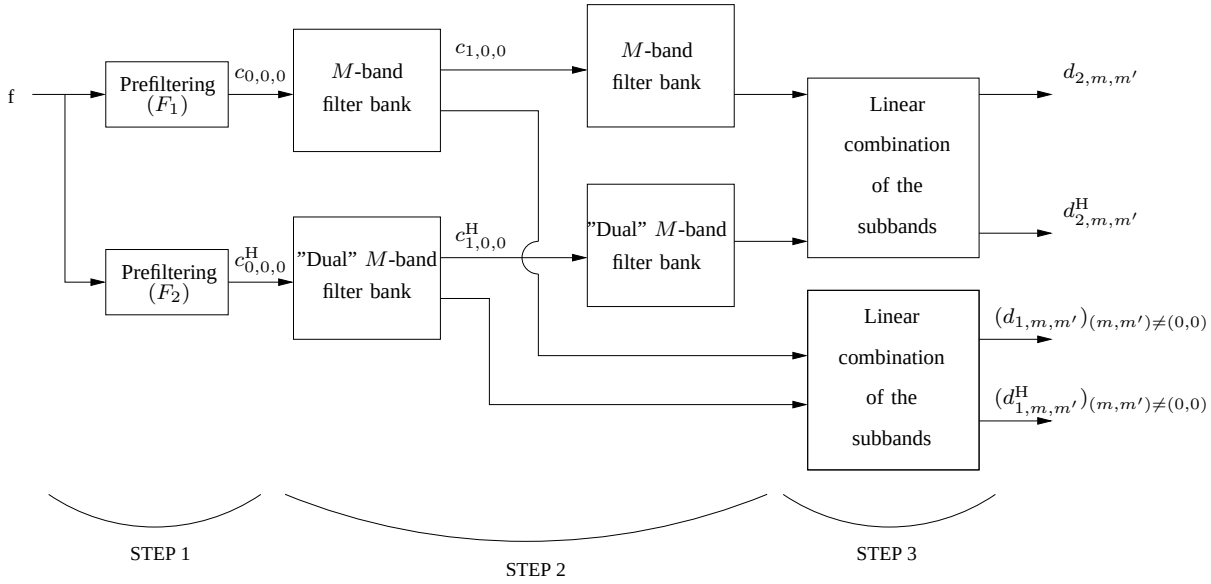

Fig. 3. M-band dual-tree decomposition scheme over 2 resolution levels.

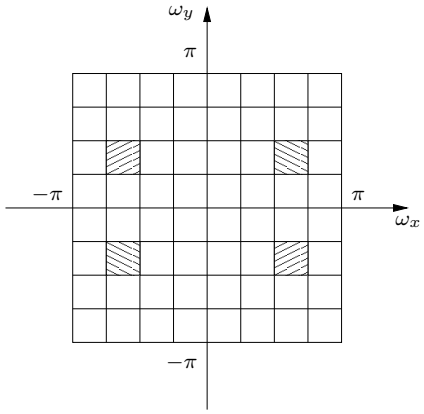

Fig. 4. Direction selectivity in the 2D frequency plane when $M = 4$, $j = 1$ and $(m, m') = (2, 1)$. The two hachured areas, which are "mixed" in the original M-band wavelet decomposition, can be separated by using tensor products of analytic/anti-analytic wavelets.

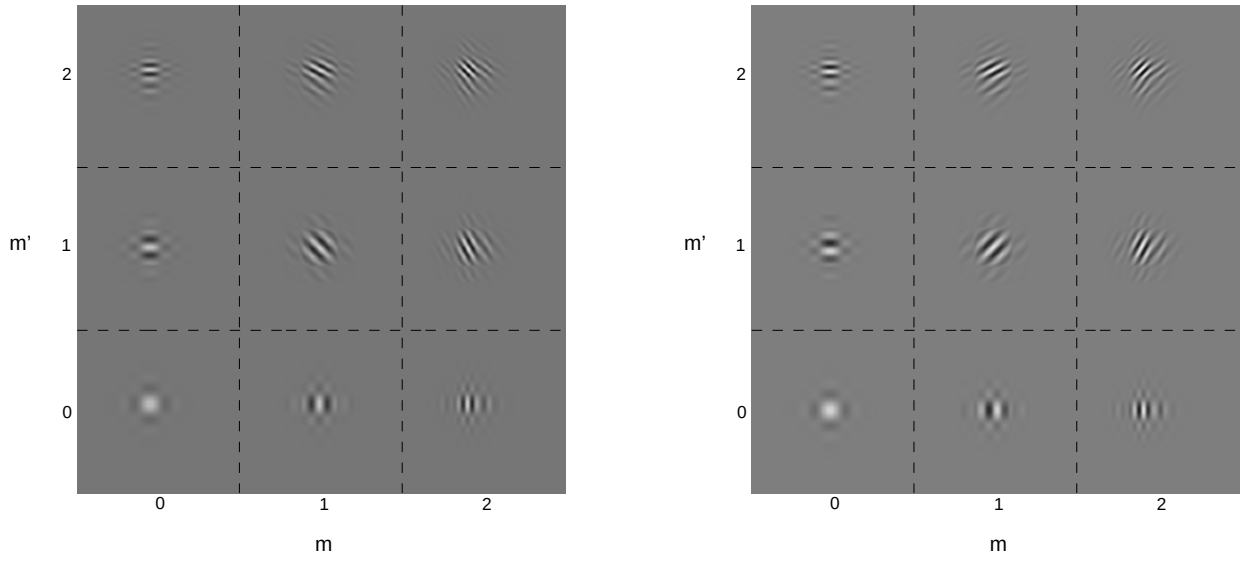

Fig. 5. Functions $(\Psi^{a}_{m,m'}(x,y))_{0\leq m,m'\leq 2}$ (on the left) and $(\Psi^{\bar{a}}_{m,m'}(x,y))_{0\leq m,m'\leq 2}$ (on the right). These functions are derived from 3-band Meyer's wavelets and their associated dual functions.

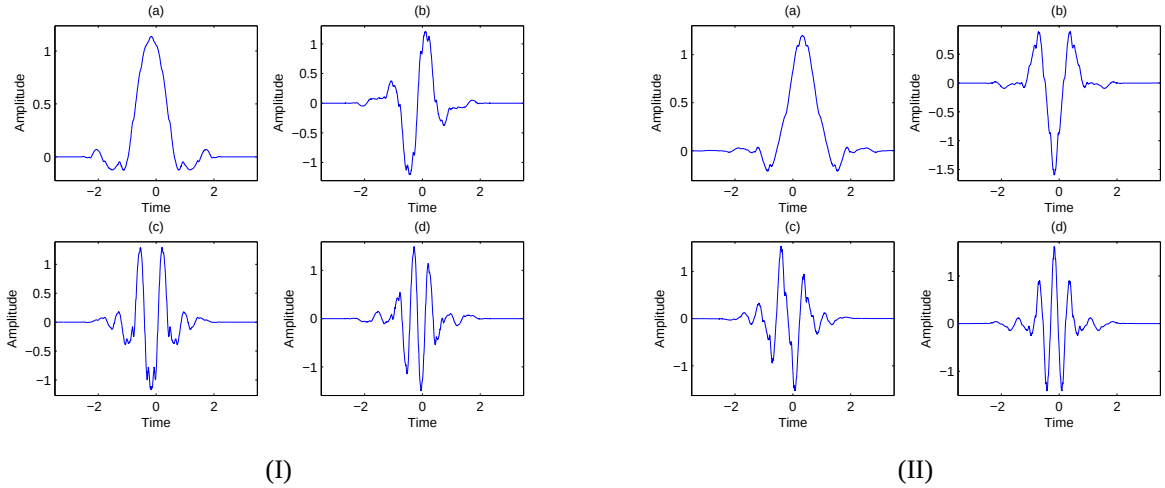

Fig. 6. (I): (a) Scaling function ψ_0 and (b) wavelet ψ_1, (c) wavelet ψ_2, (d) wavelet ψ_3 and (II): (a) Scaling function ψ_0^{H} and (b) wavelet ψ_1^{H}, (c) wavelet ψ_2^{H}, (d) wavelet ψ_3^{H} with filters derived from [25]. These functions have been generated using the scaling equations (1) and (6) in the frequency domain.

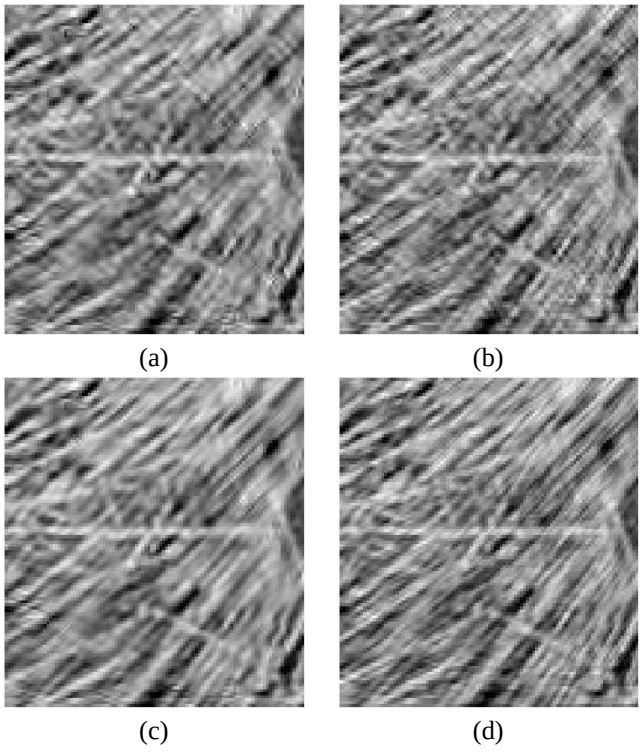

Fig. 7. Denoising results for a cropped version of the texture using Bivariate Shrinkage and: (a) DWT $M = 2$; (b) DWT $M = 4$; (c) DTT $M = 2$; (d) DTT $M = 4$.

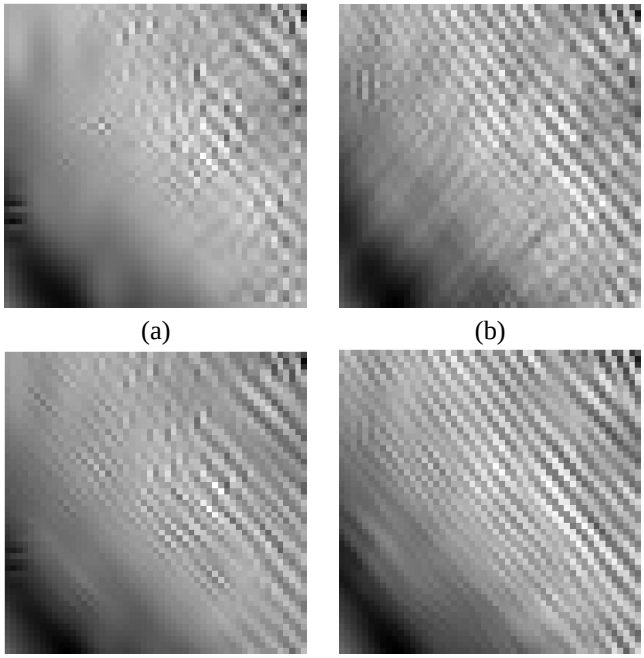

Fig. 8. Denoising results for a cropped version of "Barbara" using Bivariate Shrinkage and: (a) DWT $M = 2$; (b) DWT $M = 4$; (c) DTT $M = 2$; (d) DTT $M = 4$.

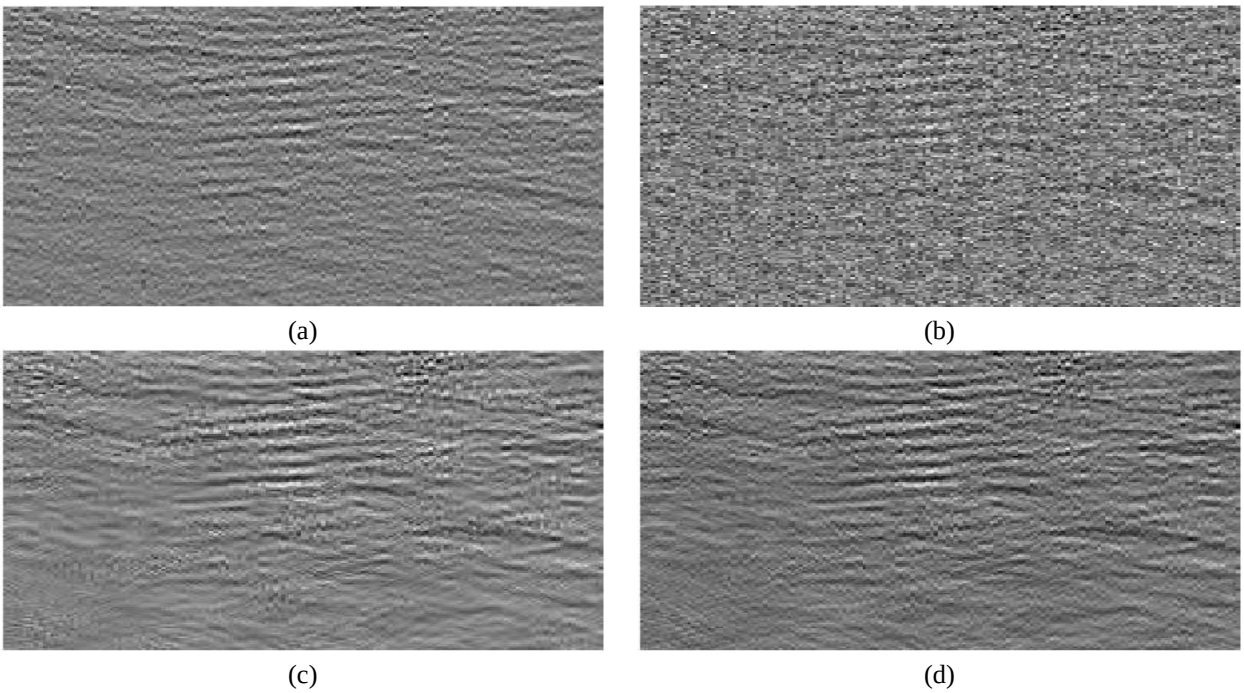

Fig. 9. Seismic data and denoising results using Neighblock: (a) Original data; (b) Noisy data; (c) DTT $M = 2$; (d) DTT $M = 4$.

	SNR$_{init}$ = 7.71 dB				SNR$_{init}$ = 5.71 dB				SNR$_{init}$ = 3.71 dB			
	Visu	SURE	Biv	NB	Visu	SURE	Biv	NB	Visu	SURE	Biv	NB
DWT $M = 2$	5.44	10.07	10.37	10.72	4.36	8.70	9.02	9.40	3.37	7.49	7.75	8.14
DWT $M = 3$	5.57	10.25	10.38	10.86	4.53	8.82	9.01	9.52	3.62	7.52	7.72	8.24
DWT $M = 4$	5.53	10.25	10.38	10.94	4.43	8.83	9.03	9.59	3.44	7.65	7.75	8.31
DTT $M = 2$	6.67	10.67	10.85	11.01	5.51	9.38	9.54	9.70	4.39	8.12	8.29	8.46
DTT $M = 3$	6.72	10.80	10.93	11.19	5.54	9.47	9.60	9.85	**4.54**	8.15	8.33	8.57
DTT $M = 4$	**6.91**	**10.91**	**10.96**	**11.31**	**5.64**	**9.50**	**9.65**	**9.98**	4.48	**8.28**	**8.40**	**8.69**
DWT $M = 2$	4.78	9.71	9.99	10.49	3.94	8.56	8.78	9.30	3.13	7.41	7.60	8.12
DWT $M = 3$	5.18	9.96	10.29	10.80	4.29	8.59	8.95	9.51	3.49	7.50	7.68	8.26
DWT $M = 4$	5.20	10.04	10.40	10.90	4.22	8.78	9.04	9.59	3.32	7.63	7.75	8.32
DTT $M = 2$	5.91	10.33	10.53	10.86	4.98	9.15	9.32	9.66	4.04	8.04	8.14	8.48
DTT $M = 3$	6.23	10.45	10.87	11.17	5.25	9.22	9.56	9.87	**4.37**	8.06	8.29	8.60
DTT $M = 4$	**6.52**	**10.62**	**10.99**	**11.31**	**5.40**	**9.45**	**9.68**	**10.00**	4.33	**8.23**	**8.42**	**8.73**

TABLE I

DENOISING RESULTS ON TEXTURE IMAGE FOR DIFFERENT INITIAL SNR'S. IN THE TOP PART OF THE TABLE, THE VARIANCE IS ASSUMED TO BE KNOWN AND IN THE BOTTOM ONE, IT IS ESTIMATED. THE CONSIDERED ESTIMATORS ARE SURESHRINK (SURE) [35], NEIGHBLOCK (NB) [37], BIVARIATE SHRINKAGE (BIV) [38] AND VISUSHRINK (VISU).

	SNR$_{init}$ = 5.67 dB				SNR$_{init}$ = 4.17 dB				SNR$_{init}$ = 2.67 dB			
	Visu	SURE	Biv	NB	Visu	SURE	Biv	NB	Visu	SURE	Biv	NB
DWT $M = 2$	8.67	12.21	13.27	13.44	8.18	10.90	12.30	12.49	7.83	10.15	11.37	11.57
DWT $M = 3$	9.65	12.18	13.32	13.52	9.06	11.13	12.41	12.59	8.53	10.43	11.54	11.68
DWT $M = 4$	9.65	12.60	13.37	13.65	9.01	11.03	12.51	12.73	8.42	10.39	11.68	11.83
DTT $M = 2$	9.38	12.89	13.76	13.69	8.73	11.93	12.79	12.74	8.25	10.88	11.84	11.80
DTT $M = 3$	10.45	12.80	13.99	13.83	9.66	11.69	13.06	12.88	8.97	10.95	12.15	11.93
DTT $M = 4$	**10.80**	**13.32**	**14.16**	**14.01**	**10.05**	**12.28**	**13.31**	**13.07**	**9.35**	**11.20**	**12.47**	**12.15**
DWT $M = 2$	8.63	12.19	13.25	13.50	8.16	10.89	12.28	12.55	7.82	10.14	11.35	11.62
DWT $M = 3$	9.63	12.17	13.31	13.55	9.05	11.13	12.41	12.61	8.53	10.42	11.54	11.70
DWT $M = 4$	9.62	12.55	13.37	13.68	8.99	11.04	12.51	12.76	8.41	10.39	11.68	11.86
DTT $M = 2$	9.33	12.88	13.74	13.75	8.70	11.92	12.77	12.79	8.23	10.85	11.82	11.84
DTT $M = 3$	10.43	12.78	13.99	13.85	9.65	11.70	13.06	12.89	8.97	10.96	12.14	11.94
DTT $M = 4$	**10.78**	**13.30**	**14.17**	**14.04**	**10.04**	**12.23**	**13.31**	**13.10**	**9.34**	**11.21**	**12.47**	**12.17**

TABLE II

DENOISING RESULTS ON BARBARA IMAGE FOR DIFFERENT INITIAL SNR'S. IN THE TOP PART OF THE TABLE, THE VARIANCE IS ASSUMED TO BE KNOWN AND IN THE BOTTOM ONE, IT IS ESTIMATED. THE CONSIDERED ESTIMATORS ARE SURESHRINK (SURE) [35], NEIGHBLOCK (NB) [37], BIVARIATE SHRINKAGE (BIV) [38] AND VISUSHRINK (VISU).

	SNR$_{init}$ = 4.13 dB				SNR$_{init}$ = 3.13 dB				SNR$_{init}$ = 2.13 dB			
	Visu	SURE	Biv	NB	Visu	SURE	Biv	NB	Visu	SURE	Biv	NB
DWT $M = 2$	3.17	6.66	6.78	7.46	2.83	6.05	6.19	6.87	2.51	5.48	5.64	6.30
DWT $M = 3$	3.53	7.12	7.14	7.84	3.21	6.51	6.53	7.23	2.90	5.91	5.96	6.64
DWT $M = 4$	3.60	7.52	7.47	8.16	3.24	6.91	6.83	7.53	2.91	6.31	6.23	6.93
DTT $M = 2$	3.82	7.12	7.10	7.57	3.47	6.52	6.50	6.98	3.12	5.96	5.96	6.42
DTT $M = 3$	4.15	7.49	7.42	7.92	3.79	6.91	6.82	7.31	3.46	6.28	6.25	6.72
DTT $M = 4$	**4.23**	**7.82**	**7.72**	**8.21**	**3.84**	**7.23**	**7.09**	**7.58**	**3.49**	**6.65**	**6.49**	**6.98**
DWT $M = 2$	2.56	5.19	5.73	6.76	2.34	4.92	5.37	6.34	2.11	4.64	5.03	5.92
DWT $M = 3$	3.27	6.60	6.77	7.72	3.01	6.28	6.26	7.16	2.75	5.62	5.76	6.61
DWT $M = 4$	3.50	7.51	7.36	8.16	3.17	6.88	6.74	7.54	2.86	6.29	6.15	6.94
DTT $M = 2$	3.12	5.86	5.97	6.93	2.89	5.51	5.62	6.51	2.65	4.95	5.28	6.10
DTT $M = 3$	3.84	7.07	7.04	7.84	3.55	6.56	6.52	7.27	3.27	5.97	6.02	6.72
DTT $M = 4$	**4.11**	**7.81**	**7.60**	**8.23**	**3.76**	**7.22**	**6.99**	**7.60**	**3.42**	**6.64**	**6.41**	**7.00**

TABLE III

DENOISING RESULTS ON SEISMIC IMAGE FOR DIFFERENT INITIAL SNR'S. IN THE TOP PART OF THE TABLE, THE VARIANCE IS ASSUMED TO BE KNOWN AND IN THE BOTTOM ONE, IT IS ESTIMATED. THE CONSIDERED ESTIMATORS ARE SURESHRINK (SURE) [35], NEIGHBLOCK (NB) [37], BIVARIATE SHRINKAGE (BIV) [38] AND VISUSHRINK (VISU).

	Visu	SURE	Biv	NB	Visu	SURE	Biv	NB	Visu	SURE	Biv	NB
Texture	$\text{SNR}_{init} = 7.71$ dB				$\text{SNR}_{init} = 5.71$ dB				$\text{SNR}_{init} = 3.71$ dB			
symlet DWT	5.01	9.78	9.96	10.33	3.97	8.40	8.58	8.99	3.07	7.12	7.31	7.73
DW MLT	5.04	10.08	10.11	10.58	3.94	8.60	8.71	9.20	3.01	7.33	7.38	7.89
AC DWT	5.18	10.06	10.07	10.58	4.11	8.61	8.70	9.22	3.19	7.32	7.39	7.94
symlet DTT	6.59	10.64	10.85	10.91	5.36	9.36	9.55	9.61	4.24	8.16	8.32	8.38
DT MLT	6.94	**11.04**	**11.07**	**11.32**	5.56	**9.72**	**9.79**	**9.99**	4.35	**8.50**	**8.54**	8.70
AC DTT	**6.95**	10.97	11.01	11.29	**5.60**	9.69	9.74	9.97	**4.40**	8.45	8.52	**8.71**
Barbara	$\text{SNR}_{init} = 5.67$ dB				$\text{SNR}_{init} = 4.17$ dB				$\text{SNR}_{init} = 2.67$ dB			
symlet DWT	8.66	11.83	12.72	12.95	8.21	10.76	11.83	12.06	7.85	9.94	10.98	11.19
DW MLT	8.95	12.05	12.70	12.96	8.37	11.00	11.81	12.05	7.88	9.81	10.97	11.17
AC DWT	9.20	12.17	12.93	13.17	8.58	10.86	12.06	12.27	8.08	9.94	11.23	11.39
symlet DTT	9.45	12.92	13.69	13.62	8.86	11.82	12.74	12.70	8.43	10.85	11.83	11.80
DT MLT	10.49	13.29	14.15	13.98	9.67	**12.32**	13.26	13.07	8.94	11.07	12.39	12.17
AC DTT	**10.71**	**13.40**	**14.31**	**14.08**	**9.88**	12.31	**13.43**	**13.17**	**9.12**	**11.16**	**12.56**	**12.28**
Seismic	$\text{SNR}_{init} = 4.13$ dB				$\text{SNR}_{init} = 3.13$ dB				$\text{SNR}_{init} = 2.13$ dB			
symlet DWT	3.22	6.64	6.74	7.39	2.91	6.04	6.15	6.80	2.60	5.47	5.60	6.23
DW MLT	3.54	7.09	7.08	7.72	3.22	7.11	6.47	7.11	2.92	5.90	5.90	6.53
AC DWT	3.64	7.27	7.26	7.90	3.31	6.61	6.64	7.29	3.01	6.06	6.05	6.70
symlet DTT	3.99	7.22	7.25	7.63	3.64	6.65	6.66	7.05	3.31	6.11	6.12	6.50
DT MLT	4.30	8.01	7.74	8.13	3.95	7.40	7.12	7.53	3.62	6.82	6.53	6.96
AC DTT	**4.39**	**8.04**	**7.83**	**8.24**	**4.02**	**7.44**	**7.20**	**7.64**	**3.68**	**6.85**	**6.60**	**7.05**

TABLE IV

DENOISING RESULTS FOR DIFFERENT INITIAL SNR'S AND DIFFERENT WAVELETS FAMILIES. THE THREE PREVIOUS IMAGES ARE STUDIED. THE CONSIDERED ESTIMATORS ARE SURESHRINK (SURE) [35], NEIGHBLOCK (NB) [37] , BIVARIATE SHRINKAGE (BIV) [38] AND VISUSHRINK (VISU).